Population dynamics and dephasing of excitons and electron-hole pairs in polytype wurtzite/zinc-blende InP nanowires

H. P. Wagner,[1,*] M. Kaveh,[2] Q. Gao,[3] H. Tan,[3] C. Jagadish,[3] and W. Langbein[4]

[1]*Department of Physics, University of Cincinnati, Cincinnati, Ohio 45221, USA*

[2]*Department of Physics and Astronomy, James Madison University, Harrisonburg, Virginia 22807, USA*

[3]*Department of Electronic Materials Engineering, Research School of Physics and Engineering, Australian National University, Canberra ACT 2601, Australia*

[4]*School of Physics and Astronomy, Cardiff University, Cardiff CF24 3AA, United Kingdom*

(Received 29 June 2016; revised manuscript received 21 November 2016; published 18 January 2017)

We investigated the dephasing and population dynamics of electron-hole (e-h) pairs and excitons in vapor-liquid-solid grown polytype wurtzite/zinc-blende (WZ/ZB) InP nanowires (NWs) using heterodyne four-wave mixing (HFWM) in three-beam configuration at temperatures from 80 to 270 K. The photon energy of the 100 fs excitation pulses was varied to predominantly excite either mobile excitons and e-h pairs or indirect WZ/ZB excitons. The population dynamics reveal a multiexponential decay with time constants ranging over six orders of magnitude. The dynamics has been interpreted by a coupled rate equation model which considers WZ and ZB electron states, donor electron states, and band bending trapping holes to the surface. The model reproduces the essential features of the experimentally observed dynamics at different excitation energies, fluences, and lattice temperatures. Intraband thermalization is reached within 5–50 ps, after which the nonradiative recombination dominates the dynamics. Notably, the screenable surface band bending results in long-lived spatially separated carriers, causing a photogenerated, spatially separated electron and hole density which is dominating the long-lived dynamics.

DOI: 10.1103/PhysRevB.95.045305

I. INTRODUCTION

In recent years, semiconductor nanowires (NWs) have attracted significant attention because of their electronic and optical properties such as their directed charge transport capabilities [1] and optical polarization sensitivities [2–4]. Different synthetic approaches have been developed to fabricate NWs including the vapor-liquid-solid (VLS) growth [5–7], solution-liquid-solid (SLS) growth [8], and template based methods [9–11]. Due to the small radial dimensions of the NWs, the design of NW heterostructures is not limited by strain as in conventional planar molecular beam epitaxy (MBE) or metal-organic vapor phase epitaxy (MOVPE), thus enabling the fabrication of a wide variety of radial heterostructures as e.g. GaAs/AlGaAs [7], GaAs/GaP [12], and InP/InAs [13] core-shell NWs. Also, axial NW heterostructures [7,14] become feasible that comprise segments of different semiconductor material with nanometer thickness along the NW [15–17]. Another interesting type of axial heterostructure uses alternating few nanometer short segments of the same chemical material but different crystal structure as e.g. in wurtzite/zinc-blende (WZ/ZB) InP [18–20] and GaAs [21] NWs revealing a type-II band alignment.

This flexibility in NW design and growth has enabled novel device applications, including NW lasers [10,22,23], light emitting and detection devices [2,24–26], ultrahigh density transistors [27], single-electron charging devices [28,29], as well as single photon emitters [15,30,31] and detectors [32]. However, due to their large surface-to-volume ratio, the electronic and optical properties of semiconductor NWs are susceptible to surface states and defects. It is therefore important to understand the processes which determine the carrier relaxation and transfer dynamics in these novel nanostructures.

Time-resolved photoluminescence (TRPL) spectroscopy using time-correlated single photon counting (TCSPC) measures the dynamics of carrier transitions with a time resolution in the tens of picoseconds. Time-resolved photoluminescence measurements showed exciton recombination times faster than 80 ps [7] for ZB GaAs NWs and of ∼1 ns for GaAs/AlGaAs core-shell NWs at 20 K [7,33,34], revealing the influence of carrier trapping at nonradiative surface states which is reduced by passivation of the NW surface with a material of higher band gap. InP NWs of both ZB [35,36] and WZ [36,37] type instead show exciton decay times in the order of 1 ns even without a core-shell structure due to a three orders of magnitude slower surface recombination as compared to GaAs. Even longer exciton recombination times have been observed in axial polytype WZ/ZB GaAs NWs (3–8 ns) [21] and in WZ/ZB InP NWs (about 8 ns) [18], which has been attributed to spatially indirect excitons across the WZ/ZB interfaces. Photoluminescence (PL) up-conversion experiments with a time resolution of about 200 fs were used to measure the conversion times from electron-hole (e-h) pairs in WZ sections to indirect WZ/ZB excitons in InP NWs under nonresonant excitation [38]. The obtained conversion times increase with increasing NW diameter from 20 to 40 ps for 50 to 160 nm wide NWs.

The nonlinear optical technique of four-wave mixing (FWM) is a powerful method to study coherent and incoherent carrier relaxation processes down to the femtosecond timescale. Four-wave mixing is excited by two or three mutually delayed pulses [39], typically with noncollinear wave vectors generating a diffracted nonlinear response which can be directionally selected. While this method has been widely applied to two-dimensional (2D) and bulk semiconductors,

*wagnerhp@ucmail.uc.edu

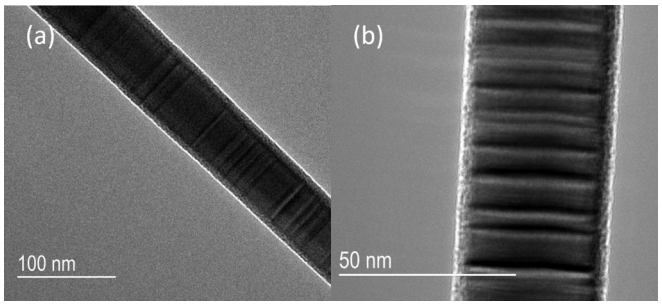

FIG. 1. (a) and (b) HRTEM images of a polytype WZ/ZB InP NW. Adjacent WZ and ZB sections are visible as bright and dark segments, respectively.

FWM experiments on epitaxially grown or etched quantum wires (QWRs) have proven to be challenging due to a reduced signal and strong Rayleigh scattering. Only a few groups reported on directional selective FWM in t-shaped GaAs QWRs [40], in wet-chemical etched III-V [41–43], and II-VI QWRs [44–46]. The more advanced technique of heterodyne FWM (HFWM) [47] combines directionally selected FWM with a highly sensitive and selective heterodyne detection [48], providing sufficient suppression of the Rayleigh scattering background.

II. EXPERIMENTAL

A. Growth of InP NWs

The polytype WZ/ZB InP NWs have been grown by the VLS technique [5–7] at a growth temperature of 450 °C and a V/III ratio of 300 on a fused silica substrate. As a growth catalyst, dispersed ∼50 nm diameter Au particles have been used, resulting in tapered NWs with an average length of 4 μm, a base diameter of 150 to 200 nm, and a tip diameter of ∼40 nm [49]. The area density of the NWs on the silica substrate is ∼4 NWs/μm^2.

High-resolution transmission electron microscopy (HRTEM) micrographs reveal a high density of stacking faults resulting in WZ and ZB sections which appear as bright or dark segments, respectively [see Figs. 1(a) and 1(b)]. The WZ and ZB section sizes range from a few tens of nanometers to 1 nm [18,38,49]. The WZ-ZB-WZ-ZB sequences define quantum wells for electrons and holes in the ZB and WZ segments, respectively, with varying confinement energies according to the length of the sections.

B. Optical characterization of InP NWs

Prior to the HFWM experiments, the NWs have been optically characterized by temperature- and intensity-dependent PL experiments [49], excited by a continuous wave (cw) He-Ne laser at 1.96 eV photon energy. A lens with a focal length of 125 mm has been used to collimate the 2 mm wide He-Ne laser beam (with Gaussian intensity profile) onto the sample, resulting in an excitation area of 2×10^{-5} cm^2. The sample was held in a closed-cycle Helium cryostat at temperatures varied between 20 and 300 K. The PL from the NW ensemble was spectrally analyzed by a monochromator and detected by a photomultiplier with a GaAs cathode.

C. HFWM experiments

The HFWM experiments were performed using Fourier-limited pulses of about 100 fs duration at 76 MHz repetition rate. In these experiments, the NWs were transferred onto a quartz crystal substrate and embedded into a polystyrene (PS) layer of a few tens of micrometers thickness by drop casting a 5% PS in toluene solution. The NWs were randomly oriented within the PS layer and tended to accumulate in small clusters, leading locally to a higher density than on the fused silica substrate. They were then covered by a second quartz substrate and mounted into a cold finger nitrogen-flow cryostat, at temperatures down to $T = 80$ K. The population dynamics of excitons and e-h pairs was studied by using three exciting pulses 1, 2, and 3 with different incident directions $\mathbf{k}_{1,2,3}$ and with zero delay ($\tau_{21} = 0$) between the pump pulses 1 and 2 and variable delay time τ_{31} of the probe pulse 3. The pulses are focused onto the NW sample to a beam diameter of 26 μm. The spectral full width at half maximum (FWHM) of the exciting Gaussian shaped pulse intensity is about 11 nm (19 meV). The pulses were spectrally tuned from $\lambda_{exc} = 830$ to 860 nm center wavelength in 10 nm steps to excite the InP NWs. Pulses 1 and 2 had equal fluences varied from 0.08 to 1.6 μJ/cm^2 (each pulse), while the fluence of pulse 3 was kept at 0.17 μJ/cm^2. The FWM signal was detected along the direction $\mathbf{k}_3 + \mathbf{k}_2 - \mathbf{k}_1$ in a square configuration in transmission geometry. To enable heterodyne detection, the pulses were frequency up-shifted with acousto-optic modulators (AOMs) by frequencies $\Omega_1/2\pi = 80$ MHz, $\Omega_2/2\pi = 79$ MHz, and $\Omega_3/2\pi = 78.8$ MHz close to the repetition rate ($\Omega_{rep}/2\pi = 76$ MHz) of the laser. The linear pulse chirp at the sample due to the AOMs and other optics has been removed by prechirping in a grating based pulse compressor, as verified using a second-order autocorrelation. The FWM signal in $\mathbf{k}_3 + \mathbf{k}_2 - \mathbf{k}_1$ direction having frequencies of $\Omega_S = \omega_0 + \Omega_3 + \Omega_2 - \Omega_1$ plus integer multiples of Ω_{rep} is subsequently interfered in a beam splitter with a reference pulse with center frequency ω_0 and arrival time $\tau_{ref} = 0$ relative to the transmitted pulse 3. The resulting signal with frequency $(\Omega_S - \Omega_{rep})/2\pi = 1.8$ MHz is measured by two high-frequency photodiodes in balanced detection, amplified by a current preamplifier (Femto DHPCA-100) and analyzed by a lock-in amplifier (SR844) using integration times of about 100 ms per point. Further details are given in the supplement of Ref. [50].

The same HFWM setup was applied to study the dephasing of excitons in the NW ensemble by varying the delay τ_{21} between pulses 1 and 2 (with pulse 2 being fixed in time). The reference pulse was delayed by τ_{ref} with respect to pulse 3. The measurements were performed at $\lambda_{exc} = 830$ nm (photon energy $hc/\lambda_{exc} = 1.493$ eV) and 840 nm (1.476 eV). To measure the photon echo (PE), the delay range τ_{ref} was scanned from −500 to 500 fs around τ_{21} with 50 fs steps. Pulse 3 was fixed at a delay $\tau_{32} = 0.7$ ps (for $\lambda_{exc} = 830$ nm) and $\tau_{32} = 1.0$ ps (for $\lambda_{exc} = 840$ nm) after pulse 2. The resulting PE signal in direction $\mathbf{k}_3 + \mathbf{k}_2 - \mathbf{k}_1$ was measured as described earlier. The heterodyne detection scheme suppresses the Rayleigh scattering by typically five orders of magnitude in field, so that it is negligible compared to the shot noise.

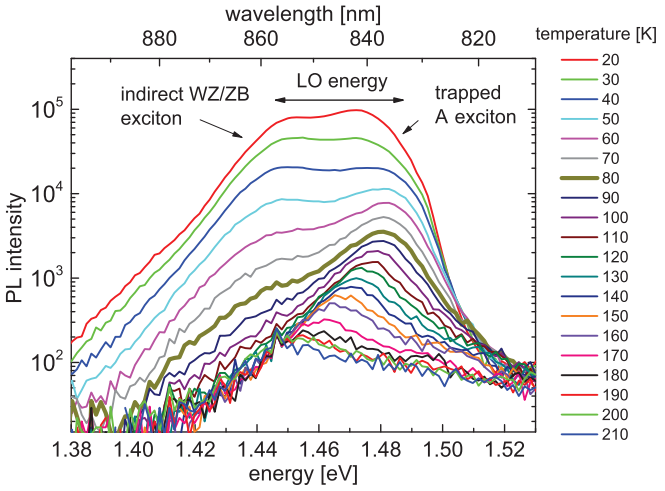

FIG. 2. PL spectra at sample temperatures T ranging from 20 to 210 K as labeled. The spectrum at 80 K is highlighted. The excitation was at 633 nm with an intensity of 8 W/cm^2.

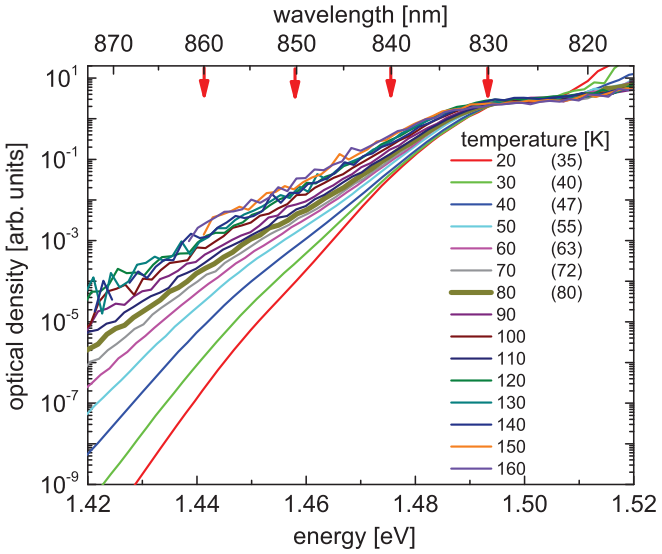

FIG. 3. ODOS as a function of energy at temperatures ranging from 20 to 160 K as labeled. The exciton density spectrum at $T = 80$ K is highlighted. The thermal band gap shrinkage was corrected as described in the text. Carrier temperatures which deviate from the lattice temperature are shown in parentheses. The red arrows indicate the excitation center wavelengths used in the HFWM experiments.

III. RESULTS AND DISCUSSION

We commence by discussing the temperature-dependent PL measurements, revealing localized indirect e-h pairs or excitons at the WZ/ZB interfaces in polytype InP NWs. Subsequently, we investigate the population dynamics and dephasing of e-h pairs and of electrons originating from ionized donors as well as relaxation processes of differently localized e-h pairs using HFWM in three-beam geometry. For a quantitative analysis of the HFWM data, we use fits with a multiexponential function and a rate-equation model describing the population dynamics of electrons and holes.

A. Optical characterization of polytype WZ/ZB InP NWs

Figure 2 shows PL spectra obtained from a polytype InP NW ensemble with an area density of about 4NWs/μm^2 at temperatures ranging from 20 to 210 K on a logarithmic scale. The sample was excited with a laser at a wavelength of 633 nm with an excitation intensity of about 8 W/cm^2. The PL spectrum at 40 K shows two emission bands centered at 1.48 eV (837 nm) and at 1.445 eV (857 nm). The emission band at 1.48 eV is attributed to weakly localized WZ A excitons where electrons and holes are localized in ZB and WZ segments, due to the type-II band alignment [18,38,49]. With increasing temperature above 60 K, the A exciton emission shifts to lower energy due to the temperature-dependent band gap shrinkage [49,51]. The emission band at about 1.445 eV, which is separated from the weakly trapped A exciton band by about the longitudinal optical (LO)-phonon energy of 42.5 meV [52,53], is attributed to an enhanced population of strongly localized indirect WZ/ZB excitons [18,54,55] due to LO-phonon assisted relaxation. This interpretation is supported by determining the optical density of states (ODOS) of WZ A excitons, ranging from weak to strong localization, from the PL. Assuming intraband thermal equilibrium, the ODOS is proportional to the product of the PL intensity and a Boltzmann factor $\exp(E/kT)$ as a function of emission energy E, as shown in Fig. 3. The data are normalized in the flat ODOS region just above the WZ bandgap, at 1.50 eV, as in this region, the carriers are mobile, and a thermal distribution can be expected. The increasing ODOS above 1.51 eV is due to the B valence band. In this analysis, we have for clarity corrected the energy for the temperature dependence of the WZ band gap by subtracting a Varshni expression $-\alpha T^2/(T+\beta)$ with parameters [49] $\alpha = 3.3 \times 10^{-4}$ eV/K and $\beta = 225$ K. For sample temperatures below 80 K, we used a carrier temperature T somewhat higher than the lattice temperature to reproduce the ODOS above the mobility edge. This temperature difference is due to noncomplete thermalization of photoexcited carriers with the lattice during their lifetime, which is relevant at low temperatures when LO-phonons are not significantly occupied, and carrier-carrier scattering can still provide a thermalization of the mobile carriers [56]. With increasing temperature, the phonon-scattering rate increases, resulting in a thermal carrier distribution above 130 K as seen by the essentially temperature-independent retrieved ODOS. The separate emission band due to the nonthermal population accordingly vanishes above 130 K (see Fig. 2). At lower temperatures instead, the steeper slopes below 1.49 eV show a subthermal population of excitons below the mobility edge. The spectra of the optical density show also the relative population enhancement about one LO-phonon energy below the mobility edge, which is attributed to LO-phonon assisted relaxation of electrons from the mobility edge into the indirect ZB sections. The assignment of the emission band at about 1.44 eV as deeply localized WZ/ZB indirect excitons is consistent with its blue shift as a function of excitation intensity [49] attributed to state filling [18] and the space-charge potential created by the indirect e-h density [57].

B. Population dynamics of excitons and e-h pairs in WZ/ZB InP NWs

To measure the population dynamics, we used HFWM experiments with zero delay ($\tau_{21} = 0$) between "pump" pulses 1 and 2 and variable delay time τ_{31} of the "probe" pulse 3. We note that excitons in InP have a binding energy of about 5 meV and are therefore mostly ionized in the investigated temperature range. We will use the term e-h pairs rather than excitons throughout when discussing the dynamics, meaning to include the bound exciton states.

1. Excitation energy dependence

The red arrows in the wavelength axis in Fig. 3 indicate the excitation center wavelengths used in the HFWM experiments. The thick lines in Figs. 2 and 3 highlight the PL and optical density spectrum at 80 K, at which the excitation energy dependence was measured. Figure 4(a) shows the normalized HFWM traces for $\lambda_{exc} = 830$ nm (1.493 eV), approximately $\Delta_M = 10$ meV above the exciton mobility edge, for different pump-pulse fluences $\phi_{1,2}$ (where fluence $\phi_1 = \phi_2$ were varied synchronously) as labeled. The inset in Fig. 4(a) shows the HFWM peak amplitude as a function of the fluence ratio $\phi_{1,2}/\phi_0$, where $\phi_0 = 1.6\,\mu J/cm^2$, which follows the expected linear dependence according to the signal being proportional to $E_1^* E_2 E_3$ with the fields $E_{1,2,3}$ of the pulses. The HFWM shows an initial decay over the first picosecond, followed by a nonexponential dynamics covering time constants from 5 ps to several tens of nanoseconds. With increasing pump fluences, we observe generally an acceleration of the decay.

Figure 4(b) shows the normalized HFWM traces for $\lambda_{exc} = 840$ nm (1.476 eV), corresponding to $\Delta_M = -7$ meV (see arrow in Fig. 3). Compared to the dynamics for $\Delta_M = 10$ meV, we find a somewhat slower decay. Figure 4(c) shows the data for $\lambda_{exc} = 850$ nm (1.458 eV), corresponding to $\Delta_M = -25$ meV. Here, the initial fast decay shows a minimum at about 100 fs with a subsequent maximum at about 200 fs. Figure 4(d) shows the data for $\lambda_{exc} = 860$ nm (1.441 eV), corresponding to $\Delta_M = -42$ meV, one LO-phonon energy, below the mobility edge, resonant to deeply localized WZ/ZB indirect e-h pairs (see Fig. 3). At this excitation energy, we observe the longest decay times. The HFWM amplitudes as a function of ratio $\phi_{1,2}/\phi_0$ shown in the insets of Figs. 4(b)–4(d) reveal similar or only slightly reduced values compared to the inset Fig. 4(a) despite the significantly reduced excitation density at lower excitation energies. We attribute this behavior to a reduced reabsorption of the HFWM signal, as the NWs are getting transparent at energies below the WZ band gap (compare Fig. 3), showing an approximately exponential decrease of the ODOS of about one order of magnitude per 20 meV.

For a quantitative evaluation of the HFWM data, we have fitted the traces with a multiexponential function with five time constants T_i and amplitudes A_i, which is the minimum number to achieve a good agreement with the experimental data. Note that the data covers four orders of magnitude between time resolution and range, and the five decay times are ranging over five orders of magnitude. The resulting order of magnitude difference between exponential decay times allows for a well-defined multiexponential fit. We also included a δ-function with amplitude A_0 to model instantaneous nonresonant virtual transitions such as two-photon absorption, Kerr effect, and relaxation processes below the temporal resolution limit. We considered that the measured HFWM data is the convolution of the multiexponential function with a Gaussian pulse intensity autocorrelation leading to a HFWM signal of

$$F_{HFWM}(\tau_{31}) = A_0 \exp\left[-\left(\frac{\tau_{31}-t_0}{T_{AC}}\right)^2\right] + \sum_1^5 A_i \exp\left[-\frac{\tau_{31}-t_0}{T_i} + \left(\frac{T_{AC}}{2T_i}\right)^2\right] \times \left(\frac{1}{\exp\left(\frac{T_{Rep}}{T_i}\right)-1} + \frac{1}{2}\left\{1 + \mathrm{erf}\left[\frac{(\tau_{31}-t_0)T_i - \frac{T_{AC}^2}{2}}{T_i\ T_{AC}}\right]\right\}\right), \quad (1)$$

with T_{AC} being the pulse intensity autocorrelation time. The pulses used are well described by a Gaussian function, as seen in the spectrum (see Fig. 7). The term which includes the pulse repetition period $T_{Rep} = (76\,\mathrm{MHz})^{-1}$ considers the buildup from previous pulses and is relevant only for decay constants of the same order or longer than T_{Rep}.

After fitting all data with free time constants, we found that we could consistently describe the data using fixed time constants T_1 to T_4 of 0.7, 5, 40, and 400 ps. The dashed curves in Fig. 4 show the corresponding fits at lowest and highest pulse fluence. The obtained amplitudes A_i are shown in Figs. 5(a)–5(d) for the different excitation wavelengths. Due to the complexity of the carrier dynamics including different scattering processes and a set of different states with different energies and decay rates, an attribution of time constants to individual processes is bound to be approximate. Notwithstanding, we propose here an interpretation, which will be backed up in the next section by simulations.

The density of photoexcited carriers $n_{eh} = \alpha\phi_{max}/(hc/\lambda)$ at maximum pulse fluence $\phi_{max} = 2\phi_0$ and excitation wavelength $\lambda = 830$ nm was estimated by using the band gap absorption coefficient of ZB InP [58] of $\alpha = 1 \times 10^4\,\mathrm{cm}^{-1}$ but considering the microscopic anisotropy of WZ InP which forbids optical transitions from the A-valence band (with symmetry Γ_9) to the conduction band (with symmetry Γ_7) for light that is polarized along the crystallographic $\hat{c}$ axis, along the NWs [59]. This anisotropy reduces the optical absorption of the randomly oriented NWs by a factor of 2/3. Furthermore, we consider the macroscopic anisotropy which is associated with the shape of the InP NWs. The mismatch of the dielectric constants between the NW and its surrounding environment reduces the absorption coefficient by

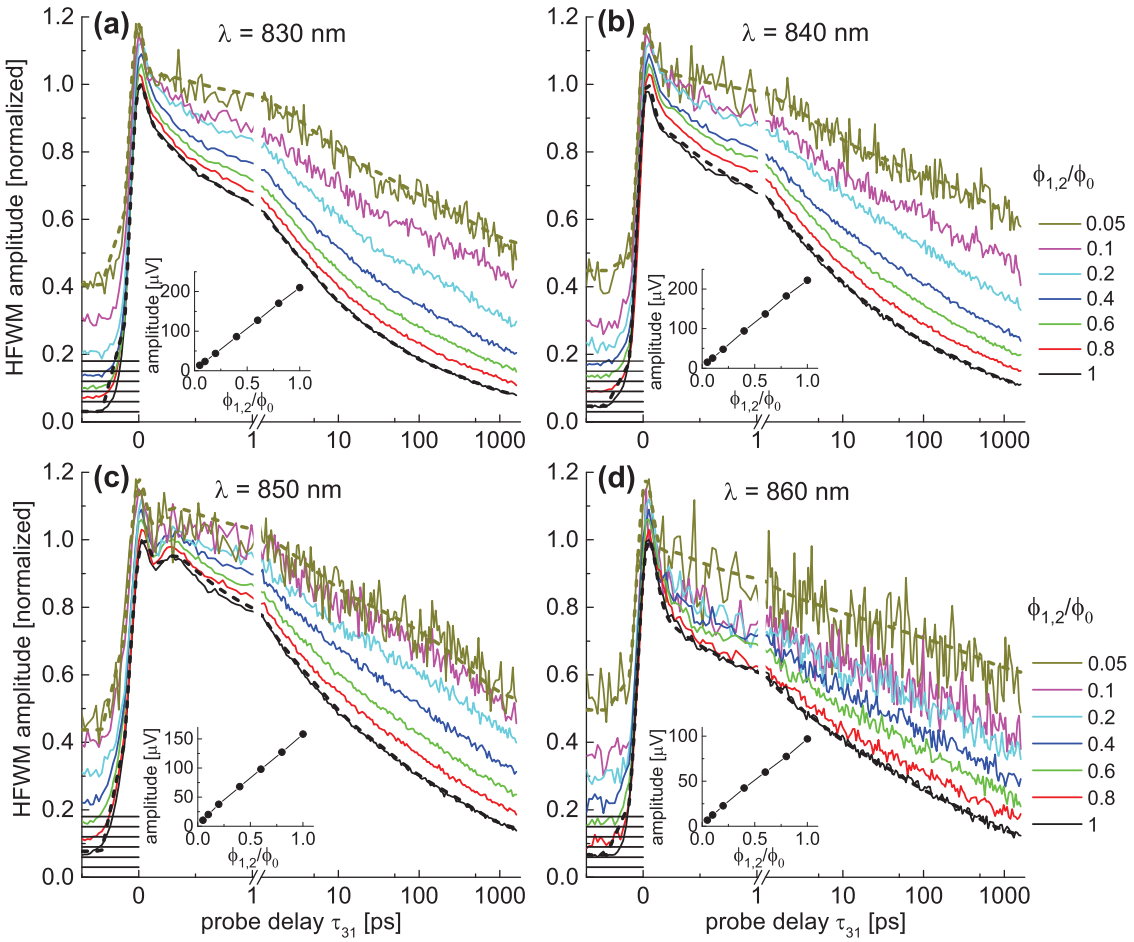

FIG. 4. Normalized HFWM amplitudes at $T = 80$ K as a function of delay τ_{13} at excitation wavelengths of (a) $\lambda_{exc} = 830$ nm, (b) 840 nm, (c) 850 nm, and (d) 860 nm for different excitation fluences $\phi_{1,2}$ as labeled. The data for different fluences are vertically offset by multiples of 0.03 for clarity, see horizontal lines. The insets show the maximum HFWM amplitude versus excitation fluences $\phi_{1,2}$. Thick dashed black and dark yellow curves represent fits using the multiexponential function given by Eq. (1) as described in the text.

an additional factor of about 1/4 [59]. At highest pulse fluence ($\phi_{max} = 3.2\mu J/cm^2$), we find a resulting e-h excitation density of about $2 \times 10^{16} cm^{-3}$.

Due to the moderate density of photoexcited carriers, Auger recombination processes [60] are not expected to be the relevant mechanism for the observed nonexponential decay. We interpret the decay in Fig. 4(a) and obtained amplitudes in Fig. 5(a) as follows: The instantaneous contribution of amplitude A_0 (shown at 100 fs) is assigned to nonresonant virtual processes. The time constant of 0.7 ps is attributed to the relaxation of highly excited e-h pairs to the mobility edge via carrier-carrier scattering. With decreasing excitation fluence, carrier-carrier scattering is suppressed due to the reduced density of excited e-h pairs, which can be the origin of the observed reduction of amplitude A_1. Processes relating to the time constant of 5 ps are attributed to the relaxation of electrons from the mobility edge into ZB regions via acoustic and LO-phonon emission. This process is responsible for the observed nonthermalized PL enhancement one LO-phonon energy below the mobility edge shown in Figs. 2 and 3. The InP NWs show a background n doping [61] with a concentration of about $10^{16} cm^{-3}$, resulting in a background electron density and corresponding ionized donors. Most of these electrons are expected to be trapped in the ZB sections due to the conduction band alignment. Intraband excitation of these electrons by the pump pulses leads to a modulation of the refractive index in the NWs giving rise to an additional HFWM signal. The intraband excited electrons, which have a large excess energy, relax via carrier-carrier scattering and LO-phonon emission towards the mobility edge on a timescale of less than 100 fs, described by A_0. Later, acoustic phonon assisted relaxation and thermalization will contribute to the HFWM amplitudes A_1 and A_2. The dynamics described by the time constant of 40 ps could be due to the thermalization of electrons between the spatially separated states such as WZ/ZB or holes between mobile and surface states. Note that, at a temperature of 80 K, a significant redistribution of the PL intensity towards thermalization is observed in Fig. 3. The longer time constants T_4 of 400 ps and T_5 ranging from 10 to 30 ns should be beyond thermalization and thus related to recombination. This recombination is dominantly nonradiative, as can be seen by the about 50 times reduction of the PL from 20 to 80 K. Nonradiative recombination is typically explained by deep traps and described as monomolecular, especially in the presence of a background doping providing a majority carrier type, electrons in the present case. The presence of a

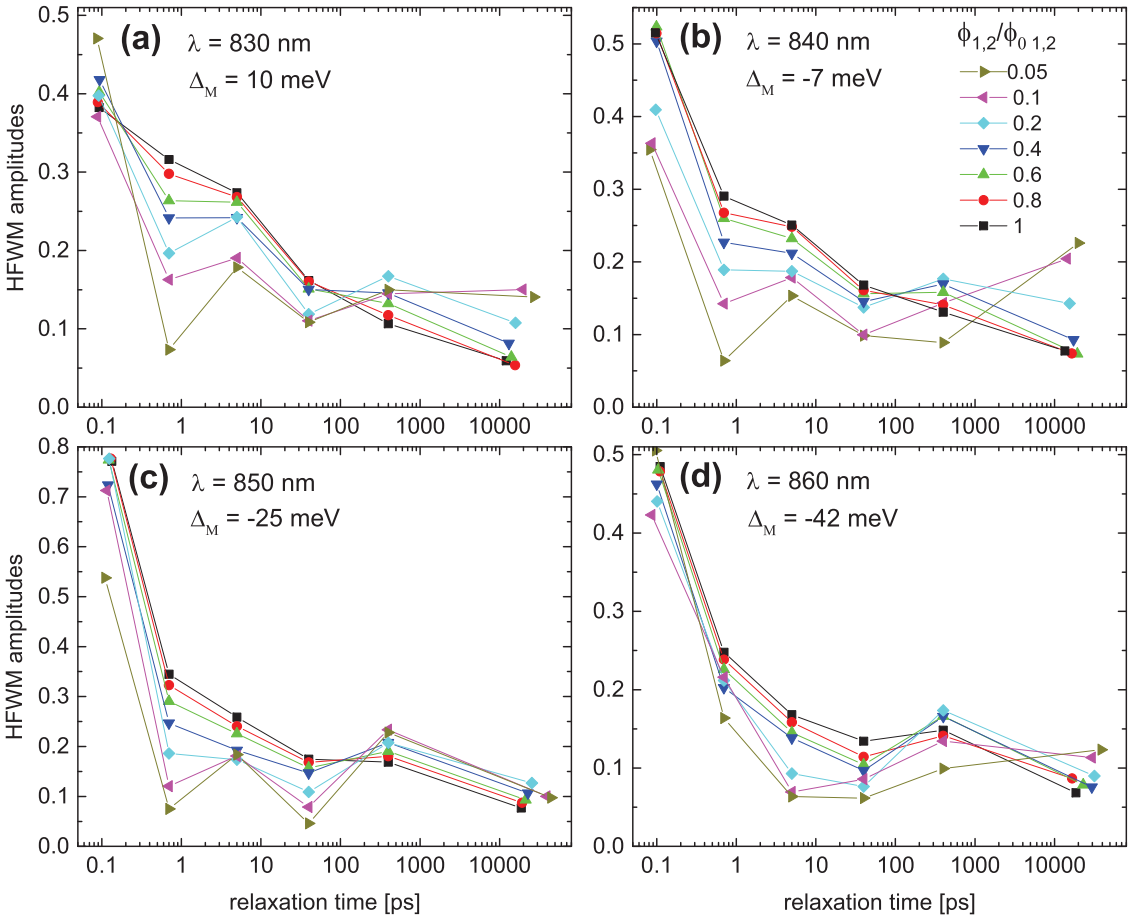

FIG. 5. Amplitudes A_i of exponential decays with time constants T_i for different excitation fluences $\phi_{1,2}$ as labeled at a sample temperature of 80 K, from fits of Eq. (1) to the HFWM at excitation wavelengths λ_{exc} of (a) 830 nm, (b) 840 nm, (c) 850 nm, and (d) 860 nm.

wide distribution of time constants for this process requires a spatial separation of the minority carriers, the holes, from the electrons. This can be provided by an upward band bending close to the NW surface due to negative surface charges [49], which leads to a spatial separation between holes at the NW surface and electrons in the NW center, with small wave function overlap and consequently small recombination rates, which is consistent with the low surface recombination velocity found in InP NWs [61]. The relaxation time T_5 decreases with increasing excitation fluence, which could be due to enhanced thermal activation of the surface trapped holes resulting from the screening of the band bending by the trapped hole density.

Moving the excitation pulses to smaller energies, the interband transitions create dominantly indirect, localized e-h pairs of exponentially decreasing optical density (see Fig. 3), and intraband excitation of resident electrons becomes more important in the initial dynamics in the first 10–100 ps before intraband thermalization.

For $\Delta_M = -7$ meV [Fig. 5(b)], the 0.7 ps contribution is reduced, otherwise a similar dynamics is found. For $\Delta_M = -25$ meV [Fig. 5(c)], the excitation of indirect WZ/ZB e-h pairs is dominating, and the initial decay shows a minimum at approximately 100 fs, which is attributed to the interband excitation of the resident electrons in the ZB trapping sites, blocking the probed transitions. Their intraband excitation results in an induced absorption, providing a HFWM amplitude destructively interfering with the amplitude due to absorption bleaching by resonantly excited e-h pairs. At higher or lower Δ_M, this effect is likely of too low strength to be visible, due to the lower occupation or the lower transition strength, respectively. In these cases, the signal resulting from the intraband absorption is predominantly a refractive index change (phase modulation), which is in quadrature to the absorption bleaching by resonantly excited e-h pairs, consistent with the absence of the minimum. To take into account the effect of the resident electrons for $\Delta_M = -25$ meV, we added an exponential function with negative amplitude A_6 into Eq. (1) and fixed its relaxation time to $T_6 = 50$ fs. The resulting fits for highest and lowest pump fluences are given as dashed curves in Fig. 4(c). For $\Delta_M = -42$ meV [Fig. 5(d)], the excitation density of mobile e-h pairs is negligible. The observed initial dynamics are therefore created dominantly by nonresonant virtual transitions and intraband excitation of resident electrons in the ZB sections. The slower dynamics relate to the relaxation of the remaining interband excitation.

2. *Temperature dependence*

To study the role of phonon-assisted processes in more detail, we performed additional measurements at sample temperatures of 150, 210, and 270 K. The excitation wave-

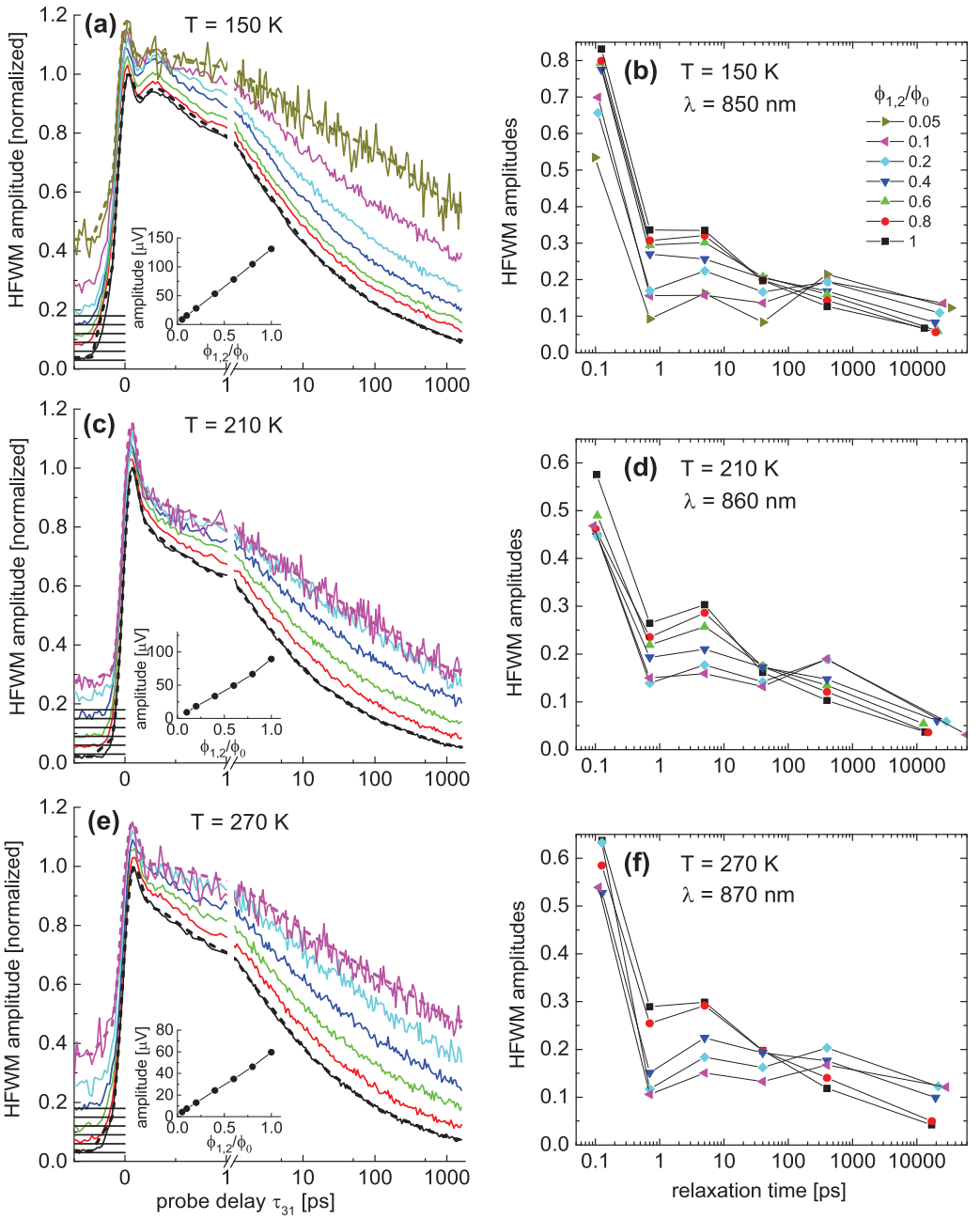

FIG. 6. Left: Normalized HFWM amplitudes at (a) $T = 150$ K, (c) 210 K, and (e) 270 K as a function of delay τ_{31} at excitation wavelengths of $\lambda_{exc} = 850$, 860, and 870 nm, respectively, for different excitation fluences $\phi_{1,2}$. The data for different fluences are vertically offset by multiples of 0.03 for clarity, see horizontal lines. The insets show the maximum HFWM amplitude versus excitation fluences $\phi_{1,2}$. Thick dashed curves represent fits using the multiexponential function given by Eq. (1). Right panel: Amplitudes A_i of exponential decays with time constants T_i at sample temperatures of (b) $T = 150$ K, (d) 210 K, and (f) 270 K for different excitation fluences $\phi_{1,2}$ as labeled, obtained by fitting the HFWM amplitudes with Eq. (1).

length was adjusted for each temperature to compensate the temperature-induced band gap shrinkage (see Fig. 2 and Ref. [49]). Figure 6(a) shows the HFWM at 150 K for $\lambda_{exc} = 850$ nm, $\Delta_M \sim -13$ meV. A similar dynamics as for $T = 80$ K, $\Delta_M \sim -25$ meV is found, including the initial minimum attributed to the intraband excitation of the trapped electrons in the ZB sections. The occurrence of the minimum despite the about 10 meV higher Δ_M can be related to an increase of the average trapped electron energy due to thermal activation. The maximum HFWM amplitude value [see inset in Fig. 6(a)] is slightly decreased compared to $T = 80$ K, $\Delta_M \sim -25$ meV [see inset of Fig. 4(c)]. Figure 6(b) shows the amplitudes extracted from Fig. 6(a) using Eq. (1), their general interpretation remains as described earlier.

The results for $T = 210$ K and $\lambda_{exc} = 860$ nm, $\Delta_M \sim -10$ meV, are given in Figs. 6(c) and 6(d). Due to the increased thermal activation of electrons from the WZ/ZB traps, the induced absorption peak is no longer noticeable. The long

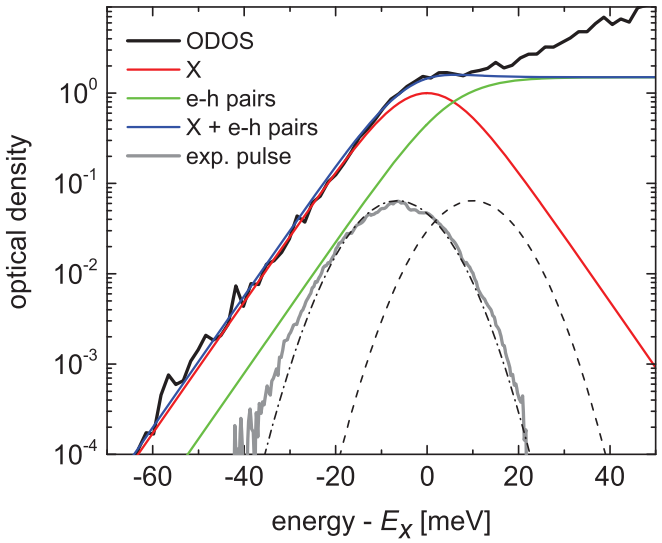

FIG. 7. ODOS (black line) as a function of energy relative to the center energy E_X of the broadened exciton band. The red, green, and blue curves are modeled exciton, continuum absorption, and the resulting total absorption, respectively. Also shown is the spectrum of the excitation pulse at $\lambda_{exc} = 840$ nm (gray curve) as well as spectra of Gaussian model pulses at $\lambda_{exc} = 830$ and 840 nm (dashed and dash-dotted curves).

lifetimes T_5 are reduced, and the maximum values of the HFWM signal are about half of those at 80 K, $\Delta_M \sim -7$ meV [see Fig. 4(b)].

The results for $T = 270$ K and $\Delta_M \sim -10$ meV are given in Figs. 6(e) and 6(f). The amplitude A_5 with long lifetime T_5 is further reduced, and the broadening of the spectral response leads to a further reduction of the maximum HFWM amplitudes.

C. Dephasing of excitons in WZ/ZB InP NWs

To study the dephasing of excitons in the WZ/ZB NWs, PE experiments were performed at Δ_M of 10 and -7 meV. The total pump-pulse fluence $\phi = \phi_1 + \phi_2$ was set to be 0.64 and 1.6 μJ/cm^2, respectively. The density of photoexcited carriers was estimated by the overlap integral of Gaussian shaped excitation pulses (with center energy E_0 and a FWHM of $\Delta E = 19$ meV) with the ODOS spectrum of InP NWs obtained at $T = 140$ K (from Fig. 3), where the photoexcited carriers are thermalized. The ODOS spectrum is shown as a black line in Fig. 7 as a function of energy relative to exciton center energy $E_X = 1.483$ eV. The measured excitation pulse spectrum with center energy 1.476 eV (840 nm) as well as modeled Gaussian pulses at center energies 1.476 eV (840 nm) and 1.493 eV (830 nm) are given in Fig. 7 as a full gray and black dashed and dash-dotted curves, respectively. To distinguish the excitation of excitons from that of e-h pairs, the optical absorption due to excitons was modeled with a broadened exciton resonance $\alpha_X(E) \propto \mathrm{sech}^2[1.76\,(E - E_X)/\Delta E_X]$ with a broadening of $\Delta E_X = 21$ meV shown as a red curve in Fig. 7. The absorption of continuum states was modeled by convoluting the unit step function $\theta[E - (E_X + E_b)]$ with the exciton function shifted by the exciton binding energy of $E_b = 5$ meV, resulting in a free carrier absorption $\alpha_{eh}(E) \propto 1 + \tanh\{1.76\,[E - (E_X + E_b)]/\Delta E_X\}$ (green curve in Fig. 7). The total absorption spectrum of excitons and e-h pairs $\alpha(E) = c_1 \cdot \alpha_X(E) + c_2 \cdot \alpha_{eh}(E)$ was then adjusted to match the ODOS spectrum as shown as a blue curve in Fig. 7. The remaining deviation at higher energies is due to the onset of the absorption due to the B-valence band and is not relevant for the excitation spectra used.

At excitation pulses at $\lambda_{exc} = 830$ nm ($\Delta_M = 10$ meV), we find a ratio of the pulse overlap integral with excitons O_X and e-h pairs O_{eh} to be $O_X/O_{eh} = 0.54$, so that 35% of the generated pairs are excitons. Using the previous estimate relating a pulse fluence of 3.2 μJ/cm^2 to a pair density of 2×10^{16} cm^{-3} (see Sec. III B 1.), a pulse fluence of 0.64 μJ/cm^2 is then estimated to result in an exciton and e-h pair density of about 1.4×10^{15} and 2.6×10^{15} cm^{-3}, respectively. For $\lambda_{exc} = 840$ nm ($\Delta_M = -7$ meV), we find an overlap integral ratio of $O_X/O_{eh} = 2.26$, thus about 70% of photoexcited pairs are excitons. Using the relative change of O_X and O_{eh} compared to $\lambda_{exc} = 830$ nm, we find the density of excitons of 4.3×10^{15} cm^{-3} and e-h pairs of 1.3×10^{15} cm^{-3} at a pulse fluence of 1.6 μJ/cm^2. Using these densities, we estimated the expected exciton dephasing time T_{coh} using the relationship

$$\frac{1}{T_{coh}} = \gamma_{bg} + \gamma_{ac} T + \gamma_{LO} \frac{1}{\exp\left(\frac{E_{LO}}{kT}\right) - 1} + \gamma_{XX} N_X + \gamma_{Xeh} N_{eh}. \quad (2)$$

In Eq. (2), the dephasing rate γ_{bg} accounts for the background dephasing due to scattering of excitons with impurities and defects and radiative decay, γ_{ac} is the acoustic phonon scattering parameter, γ_{LO} is the LO-phonon scattering parameter, the factor $\{\exp[E_{LO}/(kT)] - 1\}^{-1}$ describes the thermal LO-phonon population with k being the Boltzmann constant and E_{LO} being the LO-phonon energy. γ_{XX} is the exciton-exciton scattering parameter with N_X being the generated exciton density, and γ_{Xeh} is the exciton-e-h-pair scattering parameter with generated e-h pair density N_{eh}. Using parameters $\gamma_{bg} = 0.11$ ps^{-1}, $\gamma_{ac} = 0.007$ ps^{-1} K^{-1}, and $\gamma_{LO} = 21$ ps^{-1} from measurements on GaAs quantum wells [62] and $\gamma_{XX} = 1.6 \times 10^{-4}$ cm^3 s^{-1} and $\gamma_{Xeh} = 1.6 \times 10^{-3}$ cm^3 s^{-1} on undoped bulk GaAs [63], we expect dephasing times of $T_{coh} = 330$ and 450 fs for $\lambda_{exc} = 830$ and 840 nm at the applied pump fluences.

Figures 8(a) and 8(b) show 2D contour plots of the HFWM amplitude obtained from PE experiments as a function of time delay τ_{12} between pump pulses 1 and 2 and of delay τ_{3ref} of the reference pulse with respect to pulse 3. The delay of pulse 3 to pulse 2 was $\tau_{23} = 0.7$ ps for $\lambda_{exc} = 830$ nm and at $\tau_{23} = 1.0$ ps for $\lambda_{exc} = 840$ nm to suppress nonresonant responses. For dephasing times comparable or longer than the pulse duration (100 fs), a PE signal is expected in the upper quadrant as indicated by the white line in Fig. 8(a). The virtually symmetric data at both excitation wavelengths shows that the dephasing time is significantly below 100 fs, inconsistent with the above estimated T_{coh}. We attribute the observed faster dephasing to the scattering of excitons with the electron background density resulting from a donor concentration in the order of 1×10^{16}cm^{-3} [61]. Using γ_{Xeh} as given above, the background density results in a dephasing

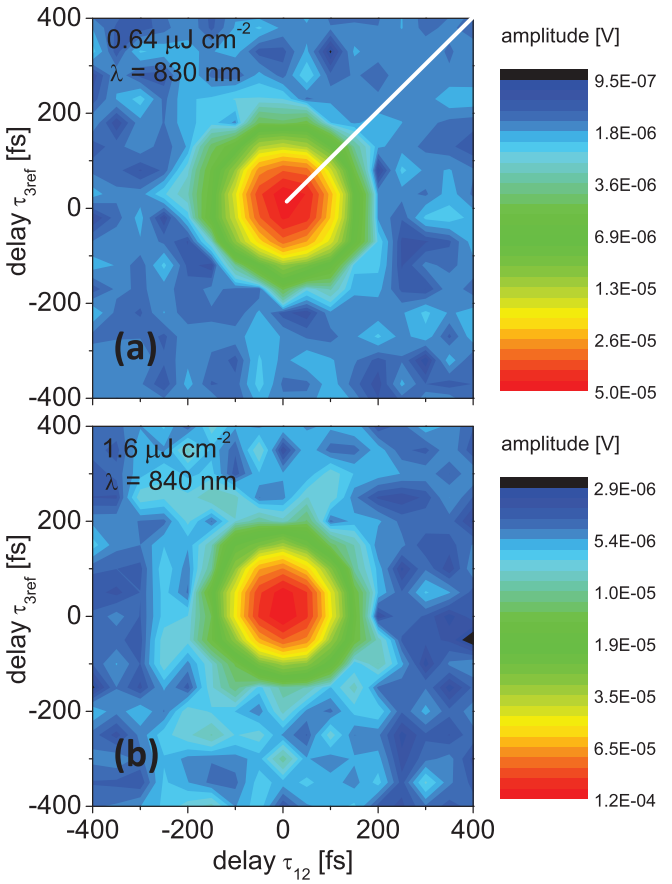

FIG. 8. 2D contour plot of HFWM amplitudes obtained from of the PE experiment. (a) Excitation wavelength of $\lambda_{exc} = 830$ nm, pump pulse fluence 1.6 μJ/cm^2 and (b) of $\lambda_{exc} = 840$ nm, 0.64 μJ/cm^2, on logarithmic color scales as given. The white line in the upper quadrant in (a) indicates where a PE signal would be expected.

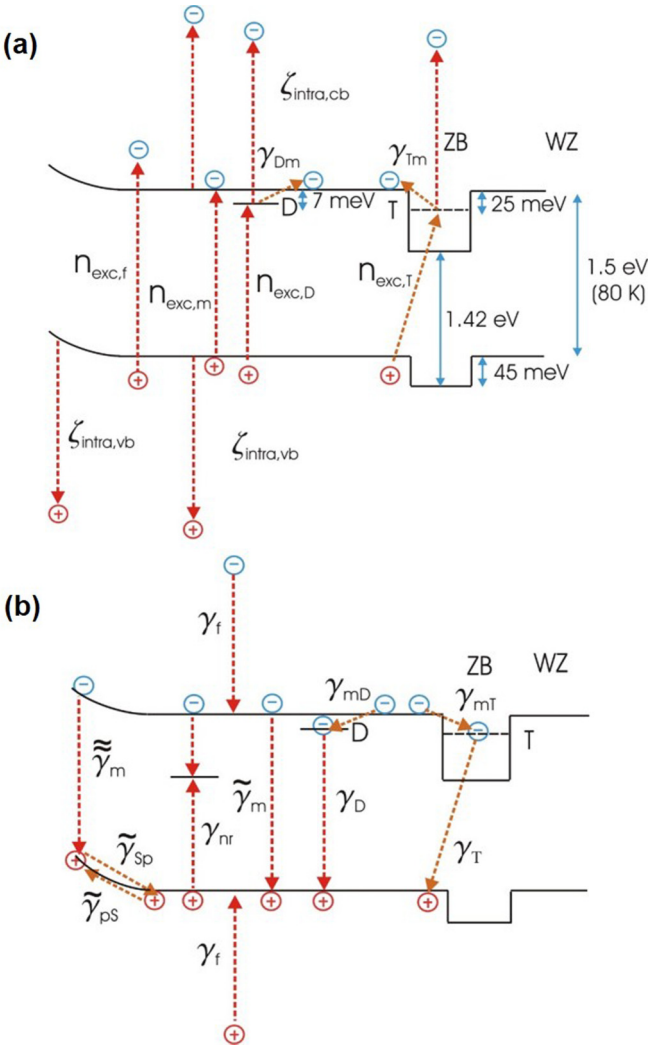

FIG. 9. Schematic sketch of all considered (a) excitation and (b) relaxation/recombination paths used in the model as described in the text.

time of 60 fs by exciton-electron scattering, consistent with the measurements. Note that the broadening of about 21 meV in the absorption model corresponds to a dephasing time of about 60 fs (FWHM $= \hbar/T_2$), consistent with the above estimate. The presence of background electrons is also affecting the population dynamics as discussed earlier.

D. Modeling of the population dynamics

Fitting the population dynamics with Eq. (1), i.e. a sum of exponential decays, is a general way to extract the dominating time constants of the dynamics and their weight. However, it assumes exponential decays, which might not be capturing the specific physical process underlying the dynamics. For our data, taken at temperatures of 80 K or higher, we note that recombination processes are dominated by e-h pairs due to thermal ionization of excitons, and the resulting recombination is bimolecular. To interpret the data in terms of the carrier dynamics, we have therefore developed a model including the essential ingredients of the system, which are sketched in Fig. 9 in terms of (a) excitation and (b) relaxation pathways, considering WZ and ZB sections, donors, and surface traps for holes. The pathways are captured in a coupled rate equation model. The model includes (i) optical excitation of e-h pairs, (ii) optical interband excitation, (iii) intraband relaxation and activation respecting detailed balance, (iv) bimolecular radiative, and (v) monomolecular nonradiative hole recombination. The coupled rate equations are given by

$$\frac{dn_f}{dt} = +P(t)[n_{\mathrm{exc,f}} + (n_D + n_T + n_m)\varsigma_{\mathrm{intra,cb}}] - \gamma_{fm} n_f,$$

$$\frac{dn_m}{dt} = +\gamma_{fm} n_f + \gamma_{Dm} n_D + \gamma_{Tm} n_T + P(t)(n_{\mathrm{exc,m}} - n_m \varsigma_{\mathrm{intra,cb}}) - (\gamma_{mD} + \gamma_{mT} + \tilde{\gamma}_m p_m) n_m - \gamma_{nr} p_m - \tilde{\tilde{\gamma}}_m p_S n_m,$$

$$
\begin{aligned}
\frac{dn_D}{dt} &= +\gamma_{mD} n_m + P(t)(\tilde{n}_{\mathrm{exc,D}} - n_D \varsigma_{\mathrm{intra,cb}}) - (\gamma_D p_m + \gamma_{Dm}) n_D,\\
\frac{dn_T}{dt} &= +\gamma_{mT} n_m + P(t)(n_{\mathrm{exc,T}} - n_T \varsigma_{\mathrm{intra,cb}}) - (\tilde{\gamma}_T p_m + \gamma_{Tm}) n_T,\\
\frac{dp_S}{dt} &= +\gamma_{pS} p_m - P(t) p_S \varsigma_{\mathrm{intra,vb}} - \tilde{\gamma}_{Sp} p_S - \tilde{\tilde{\gamma}}_m p_S n_m,\\
\frac{dp_m}{dt} &= +\gamma_{fm} p_f + \tilde{\gamma}_{Sp} p_S + P(t)(n_{\mathrm{exc,m}} + \tilde{n}_{\mathrm{exc,D}} + n_{\mathrm{exc,T}} - p_m \varsigma_{\mathrm{intra,vb}}) - (\gamma_D n_D + \tilde{\gamma}_T n_T + \tilde{\gamma}_m n_m + \gamma_{pS} + \gamma_{nr}) p_m,\\
\frac{dp_f}{dt} &= +P(t)[n_{\mathrm{exc,f}} + (p_m + p_S)\varsigma_{\mathrm{intra,vb}}] - \gamma_{fm} p_f. \qquad (3)
\end{aligned}
$$

The densities of electrons are separated into n_f highly excited in the conduction band, n_m at the WZ band edge, n_D bound to donors, and n_T trapped in ZB sections. The densities of holes are separated into p_f highly excited in the valence band, p_m at the WZ valence band edge, and p_S trapped at the NW surface (see Fig. 9 on the left) due to band bending. We consider excitation pulses of power $P(t) = \frac{F}{\sigma\sqrt{2\pi}} \exp(-t^2/2\sigma^2)$ with a Gaussian broadening of FWHM of $\sqrt{8\ln 2}\sigma = 100$ fs and the pulse fluence F. In the simulation, we use a unitless F, moving the units into the coefficients, with $F = 1$ referring to the highest used pump-pulse fluence $2\phi_0 = 3.2\ \mu\mathrm{J\,cm^{-2}}$. The excitation density $n_{\mathrm{exc},f}$ is describing the interband absorption at the excitation photon energy. n_f is furthermore populated by intraband absorption from n_m, n_D, and n_T, with a transition probability $\varsigma_{\mathrm{intra,cb}}$ for $F = 1$, and in the same way, p_f is populated from p_m and p_S with the probability $\varsigma_{\mathrm{intra,vb}}$ for $F = 1$, as indicated in Fig. 9(a). The electrons n_f and holes p_f relax with the rate γ_{fm} to the mobility edge as indicated in Fig. 9(b). Electrons n_m and holes p_m at the mobility edge are generated in pairs by optical excitation with the density $n_{\mathrm{exc},m}$. Holes p_m are also generated by optical excitation into donors n_D and trapped states n_T in the ZB sections with excitation densities $\tilde{n}_{\mathrm{exc},D} = n_{\mathrm{exc},D}(1 - n_D/n_{D_0})$ and $n_{\mathrm{exc},T}$, respectively. Donor state saturation was taken into account by the factor $(1 - n_D/n_{D_0})$ with n_{D_0} being the donor density in the NWs. Holes are captured at the NW surface (p_S) via diffusion and subsequent acoustic or LO-phonon emission with rate γ_{pS}. The relaxation of electrons n_m into n_D or n_T via acoustic or LO-phonon emission and carrier-carrier scattering is considered by the rates $\gamma_{mD} = \gamma_{mT} = \gamma_{ph}[1 + (n_m + p_m)/n_{\mathrm{sc}}]$, where n_{sc} is the density at which carrier-carrier and phonon-assisted scattering are comparable. Corresponding thermal activation processes respecting detailed balance are added, with rates $\gamma_{Dm} = (T/T_0)^{3/2}\tilde{\gamma}_{ph} \exp(-\Delta_D/kT)$, and $\gamma_{Tm} = 2\gamma_{ph} \exp(-\Delta_T/kT)$, respectively, where Δ_D and Δ_T denote the donor binding energy and average localization energy of electrons in ZB sections, respectively. The factor $(T/T_0)^{3/2}\tilde{\gamma}_{ph}$ in rate γ_{Dm} with $T_0 = 80$ K and $\tilde{\gamma}_{ph} = 8.5\gamma_{ph}$ models the effective density of states in the conduction band as a function of temperature (the density of donor states is independent of temperature), and the prefactor 8.5 is adjusted to provide detailed balance between electrons n_m in the conduction band with the effective mass of $0.073\,m_e$ [18] and neutral donors n_D at a background donor concentration of 10^{16} cm^{-3}. The factor 2 in the rate γ_{Tm} models the volume ratio of WZ to ZB sections which is approximately 1:2. Trapped holes p_S are thermally activated to the valence band with a rate $\tilde{\gamma}_{Sp} = 5\gamma_{pS} \exp[-\Delta_S(1 - p_S/p_{S_0})/kT]$ where the factor 5 takes into account a surface band bending which affects ~20% of the total NW volume. Δ_S is the trapping energy of holes at the surface. The density dependence of the trapping energy $\Delta_S(1 - p_S/p_{S_0})$ is modeling the screening of the surface band bending with a saturation density of p_{S_0}. The saturation of n_T has been neglected, motivated by the expected high density of states in the ZB sections of the NWs compared to the excitation densities used. We consider the bimolecular radiative recombination of n_m, n_T, and n_D with p_m using the rates $\tilde{\gamma}_m = \gamma_m(T/T_0)^{-3/2}$, $\tilde{\gamma}_T = \gamma_T(T/T_0)^{-3/2}$, and γ_D, respectively. The factor $(T/T_0)^{-3/2}$ in the rate $\tilde{\gamma}_m$ (with $T_0 = 80$ K) models the band-band radiative lifetime considering momentum conservation during radiative recombination of electrons and holes [64]. A bimolecular radiative recombination of n_m with surface holes p_S is taken into account using rate $\tilde{\tilde{\gamma}}_m = \gamma_m(T/T_0)^{-3/2} \exp[-\Delta_S(1 - p_S/p_{S_0})/kT]$ differing from the bulk rate by the reduced thermal occupation of electrons at the surface due to the band bending. The nonradiative decay between mobile electrons n_m and holes

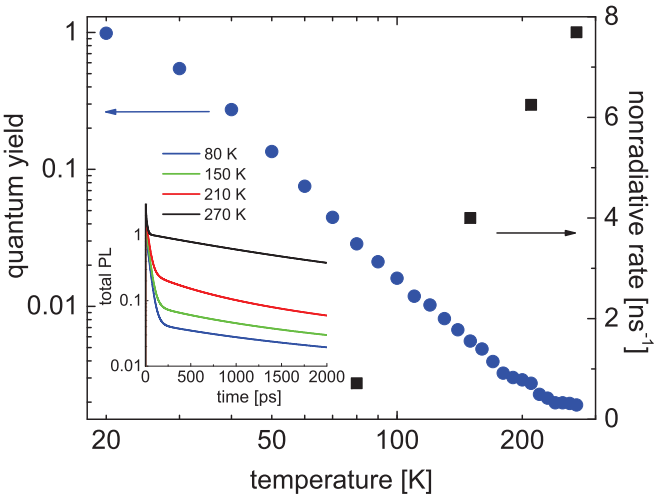

FIG. 10. Quantum yield as a function of temperature (full blue circles) obtained from the normalized spectrally integrated PL intensity from Fig. 2. The squares show the derived rates γ_{nr} for temperatures 80, 150, 210, and 270 K using Eq. (3). The inset shows the total photon emission rate for temperatures as labeled, as function of time after excitation.

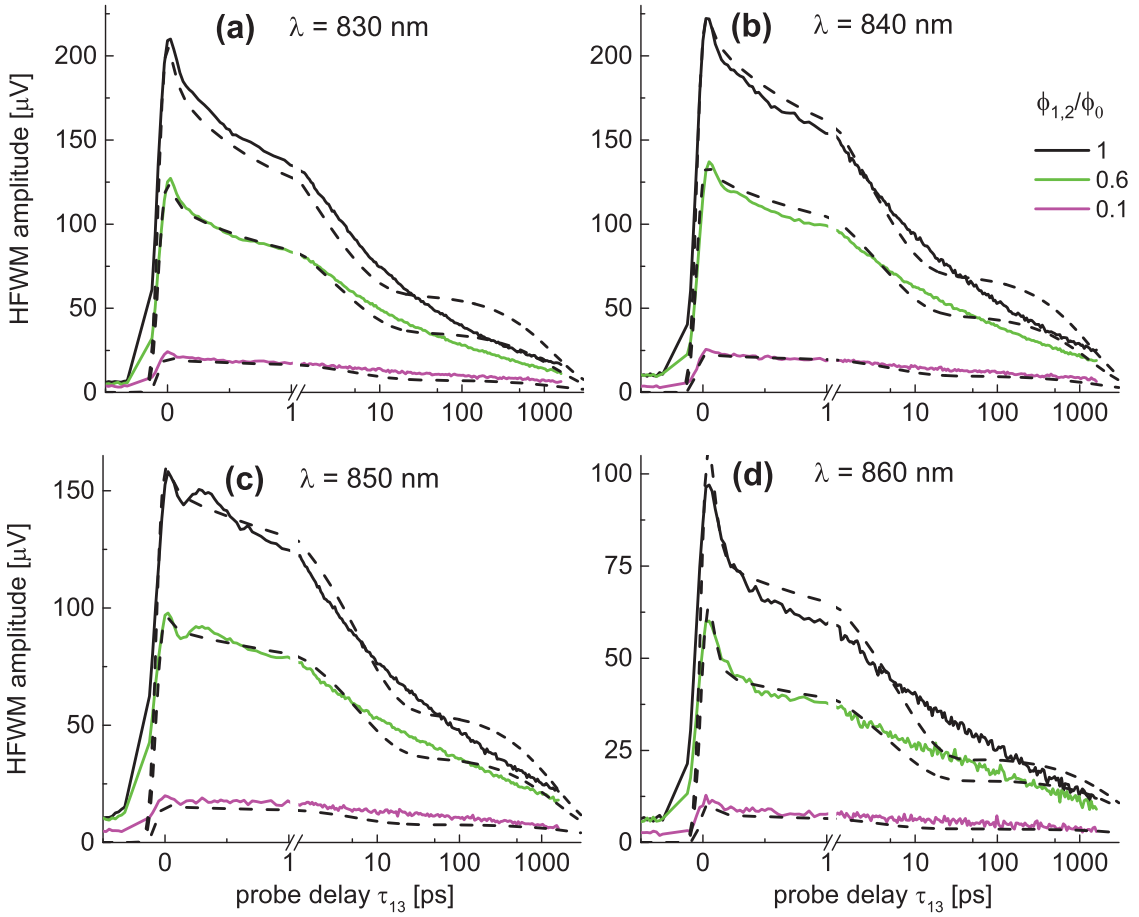

FIG. 11. Comparison of calculated HFWM traces (dashed black lines) obtained from Eqs. (3) and (4) with experimental data (full lines) acquired at excitation wavelengths (a) $\lambda_{exc} = 830$ nm, (b) 840 nm, (c) 850 nm, and (d) 860 nm at various excitation fluences $\phi_{1,2}/\phi_0$ as labeled.

p_m due to volume defects has been considered by rate γ_{nr}. It is assumed to be monomolecular in the holes, considering that, due to the high n doping, the hole trapping by the defects is expected to be the rate limiting process [see Fig. 9(b)]. Since the excitation energies in the experiments are smaller than the band gap of the ZB sections, the direct excitation of e-h pairs in the ZB sections was neglected.

Any deviation of densities $n_f(t)$, $n_m(t)$, $n_D(t)$, $n_T(t)$, $p_S(t)$, $p_m(t)$, $p_f(t)$ from quasiequilibrium values $\bar{n}_f$, $\bar{n}_m$, $\bar{n}_D$, $\bar{n}_T$, $\bar{p}_S$, $\bar{p}_m$, $\bar{p}_f$ (with $\bar{n}_f = \bar{p}_m = \bar{p}_f \approx 0$) causes a change of the susceptibility $\chi = \chi_R + i\chi_I$ where the real part accounts for changes of the phase of the transmitted field, while the imaginary part changes the amplitude. The quasiequilibrium values depend on the lattice temperature and on the repetition frequency of the exciting laser pulses and were therefore determined considering the repetition rate of 76 MHz used in the experiments. The resulting HFWM amplitude is given by

$$E_{\mathrm{FWM}} = B|C_{fe}n_f(t) + C_{me}[n_m(t) - \bar{n}_m] + C_D[n_D(t) - \bar{n}_D] + C_T[n_T(t) - \bar{n}_T] + C_S[p_S(t) - \bar{p}_S] + C_{mh}p_m(t) + C_{fh}p_f(t)|, \quad (4)$$

with complex constants C_{fe}, C_{me}, C_D, C_T, C_P, C_{mh}, C_{fh}, which account for the relative contribution of the various electron and hole dynamics types. For simplicity, we assume that (besides C_T) all constants are solely imaginary and caused by Pauli blocking, while C_T represents changes of the refraction index and thus is real. The factor B determines the overall magnitude of the calculated amplitude trace with the experimental data.

For the calculations, the relaxation rates $\gamma_f = 20\,\mathrm{ps}^{-1}$, $\gamma_{ph} = 0.14\,\mathrm{ps}^{-1}$, as well as the bimolecular recombination rates $\gamma_m = 1.25 \times 10^{-8}\,\mathrm{s}^{-1}\,\mathrm{cm}^3$, $\gamma_D = 2.5 \times 10^{-8}\,\mathrm{s}^{-1}\,\mathrm{cm}^3$, and $\gamma_T = 5 \times 10^{-10}\,\mathrm{s}^{-1}\,\mathrm{cm}^3$ have been kept constant for all excitation wavelengths and pulse fluences. The bimolecular rate $\tilde{\gamma}_m$ corresponds to an exponential decay time of 1 ns at 20 K at a hole concentration of 10^{16} cm^{-3}, compatible with earlier time-resolved measurements at low temperature [36,37,49]. The rate γ_T corresponds to an exponential decay time of 200 ns at a hole concentration of 1×10^{16} cm^{-3}, which is compatible with recent time-resolved measurements revealing lifetimes up to 100 ns at 20 K [49] and with the long decay time T_5 obtained in Sec. III B 1. For rates γ_{Dm} and γ_{Tm}, the binding energy of $\Delta_D = 7$ meV [65] and an average trapping energy $\Delta_T = 25$ meV, consistent with the observation of induced absorption [see Fig. 3(c)], were chosen. The total donor concentration was set to $n_{D_0} = 10^{16}$ cm^{-3}. The saturation density of trapped surface holes was assumed to be $p_{S_0} = 4 \times 10^{15}$ cm^{-3}. Intraband transition probabilities $\zeta_{\mathrm{intra,cb}}$ and $\zeta_{\mathrm{intra,cb}}$ were taken to be 0.05 for all excitation wavelengths. For the rate γ_{Sp}, a trapping energy of $\Delta_S = 200$ meV was

used, providing surface trapping even at 270 K, which is important to obtain the observed long lifetimes T_5 at high temperatures. The nonradiative rate γ_{nr} due to volume defects was determined matching the time-integrated photon emission $\int[(\gamma_D n_D + \tilde{\gamma}_T n_T + \tilde{\gamma}_m n_m)p_m + \tilde{\tilde{\gamma}}_m n_m p_S]dt$, calculated with Eq. (3), to the measured temperature dependence of the spectrally integrated PL intensity evaluated from Fig. 2.

A quantum yield of near unity was assumed for the PL at 20 K. The experimentally observed temperature dependence of the quantum yield is shown as blue full circles in Fig. 10. The red squares in Fig. 10 show the derived rates γ_{nr} for temperatures 80, 150, 210, and 270 K. The calculated total photon emission rate $(\gamma_D n_D + \tilde{\gamma}_T n_T + \tilde{\gamma}_m n_m)p_m + \tilde{\tilde{\gamma}}_m n_m p_S$ at low incident pump fluence ($F = 0.1$) is given in the inset of Fig. 10 at temperatures as labeled, as a function of time after excitation.

Figures 11(a)–11(d) show a comparison of model calculations (dashed lines) with experimental traces at $T = 80$ K obtained at different Δ_M and pulse fluences as labeled. For $\Delta_M = 10$ meV [Fig. 11(a)], the excitation density was divided into $n_{exc,f} = 0.4 \times 10^{16}$ cm^{-3} and $n_{exc,m} = 1.6 \times 10^{16}$ cm^{-3} at maximum pulse fluence $F = 1$. To estimate the excitation of donor bound transition, a band was introduced to the absorption model described in Sec. III C with a FWHM of 21 meV at 1.481 eV using an excitation density of $n_{exc,D} = 0.4 \times 10^{16}$ cm^{-3} at $F = 1$. For the excitation density of WZ/ZB e-h pairs, a value of $n_{exc,T} = 0.15 \times 10^{16}$ cm^{-3} was used, determined from the ODOS (see Fig. 6) integrated up to 15 meV below the gap energy. The resulting HFWM amplitude using $C_{fe} = 5.0i$, $C_{me} = 2.0i$, $C_D = 1.3i$, $C_S = 0.8i$, $C_{mh} = 0.8i$, $C_{fh} = 5.0i$, and $C_T = 0.1$ is shown in Fig. 11(a) as dashed line, for pulse ratios $\phi_{1,2}/\phi_0 = 1, 0.6$, and 0.1. In these calculations, all parameters described above as well as the proportionality factor B were kept the same with the exception of C_T, which was increased from 0.1 to 0.2 and 0.6, respectively, to achieve agreement with the experimental data. A summary of the parameters used in the simulations is given in Table I. For $\Delta_M = -7$ meV [see Fig. 11(b)], we used $n_{exc,f} = 0.1 \times 10^{16}$ cm^{-3}, $n_{exc,m} = 1.1 \times 10^{16}$ cm^{-3}, and $n_{exc,D} = 0.37 \times 10^{16}$ cm^{-3} according to the spectral overlap of the excitation pulse. The excitation density of $n_{exc,T} = 0.15 \times 10^{16}$ cm^{-3} was kept constant. The C parameters were kept the same as $\Delta_M = 10$ meV, except for C_T, which was changed to 0.2, 0.4, and 0.8 for $F = 1$, 0.6, and 0.1, respectively. The dashed lines in Fig. 11(b) show the resulting HFWM amplitude curves for different pump pulse fluences as labeled. For $\Delta_M = -25$ meV [see Fig. 11(c)], we used $n_{exc,f} = 0$, $n_{exc,m} = 0.2 \times 10^{16}$ cm^{-3}, $n_{exc,D} = 0.08 \times 10^{16}$ cm^{-3}, and $n_{exc,T} = 0.15 \times 10^{16}$ cm^{-3} according to the spectral overlap of the excitation pulse. The C parameters were kept the same as $\Delta_M = -7$ meV. For $\Delta_M = -42$ meV [see Fig. 11(d)], we used $n_{exc,f}$, $n_{exc,m}$, and $n_{exc,D}$ equal to zero and $n_{exc,T} = 0.06 \times 10^{16}$ cm^{-3} according to the reduced overlap of the excitation pulse with the ODOS tail. The C parameters were kept the same as $\Delta_M = -25$ meV, except $C_T = 0.4$, 0.7, and 1.2 was used for $F = 1$, 0.6, and 0.1, respectively.

We find a general agreement of the calculated HFWM curves with the experimental data. Remaining deviations in the dynamics at delays above 30 ps are attributed to the consideration of only one type of trapped ZB electron described by the average localization energy $\Delta_T = 25$ meV. A more realistic consideration of a distribution of trapping sites with varying trapping energies and transition rates creating a distribution of decay times would likely remedy these deviations. However, the concurrent increase in the number of fit parameters would reduce the clarity of the results.

TABLE I. Values of all parameters used to calculate the HFWM decay curves with Eqs. (3) and (4) at different excitation wavelengths, excitation fluences, and temperatures as described in the text.

Wavelength	830 nm	840 nm	850 nm	860 nm	850 nm	860 nm	870 nm
Temperature	80 K	80 K	80 K	80 K	150 K	210 K	270 K
$n_{exc,f}$ [cm^{-3}]	0.4×10^{16}	0.1×10^{16}	0	0	0	0.1×10^{16}	0.1×10^{16}
$n_{exc,m}$ [cm^{-3}]	1.6×10^{16}	1.1×10^{16}	0.2×10^{16}	0	0.7×10^{16}	1.1×10^{16}	1.1×10^{16}
$n_{exc,D}$ [cm^{-3}]	0.4×10^{16}	0.37×10^{16}	0.08×10^{16}	0	0.26×10^{16}	0.37×10^{16}	0.37×10^{16}
$n_{exc,T}$ [cm^{-3}]	0.15×10^{16}	0.15×10^{16}	0.15×10^{16}	0.06×10^{16}	0.15×10^{16}	0.15×10^{16}	0.15×10^{16}
$\zeta_{intra,vb}$	0.05	0.05	0.05	0.05	0.05	0.05	0.05
$\zeta_{intra,cb}$	0.05	0.05	0.05	0.05	0.05	0.05	0.05
γ_{fm} [ps^{-1}]	20	20	20	20	20	20	20
γ_{ph} [ps^{-1}]	0.14	0.14	0.14	0.14	0.14	0.14	0.14
γ_{pS} [ps^{-1}]	0.02	0.02	0.02	0.02	0.02	0.02	0.02
γ_{nr} [ns^{-1}]	0.71	0.71	0.71	0.71	4	6.25	7.7
γ_m [s^{-1}cm^3]	1.25×10^{-8}	1.25×10^{-8}	1.25×10^{-8}	1.25×10^{-8}	1.25×10^{-8}	1.25×10^{-8}	1.25×10^{-8}
γ_D [s^{-1}cm^3]	2.5×10^{-8}	2.5×10^{-8}	2.5×10^{-8}	2.5×10^{-8}	2.5×10^{-8}	2.5×10^{-8}	2.5×10^{-8}
γ_T [s^{-1}cm^3]	5×10^{-10}	5×10^{-10}	5×10^{-10}	5×10^{-10}	5×10^{-10}	5×10^{-10}	5×10^{-10}
C_{fe}	$5.0i$	$5.0i$	$5.0i$	$5.0i$	$5.0i$	$5.0i$	$5.0i$
C_{me}	$2.0i$	$2.0i$	$2.0i$	$2.0i$	$2.0i$	$2.0i$	$2.0i$
C_D	$1.3i$	$1.3i$	$1.3i$	$1.3i$	$1.3i$	$1.3i$	$1.3i$
C_T: $F = 1$	0.1	0.2	0.2	0.4	0.5	0.5	0.6
$F = 0.6$	0.2	0.4	0.4	0.7	0.7	0.7	0.8
$F = 0.1$	0.6	0.8	0.8	1.2	0.9	0.9	1.0
C_S	$0.8i$	$0.8i$	$0.8i$	$0.8i$	$0.8i$	$0.8i$	$0.8i$
C_{mh}	$0.8i$	$0.8i$	$0.8i$	$0.8i$	$0.8i$	$0.8i$	$0.8i$
C_{fh}	$5.0i$	$5.0i$	$5.0i$	$5.0i$	$5.0i$	$5.0i$	$5.0i$

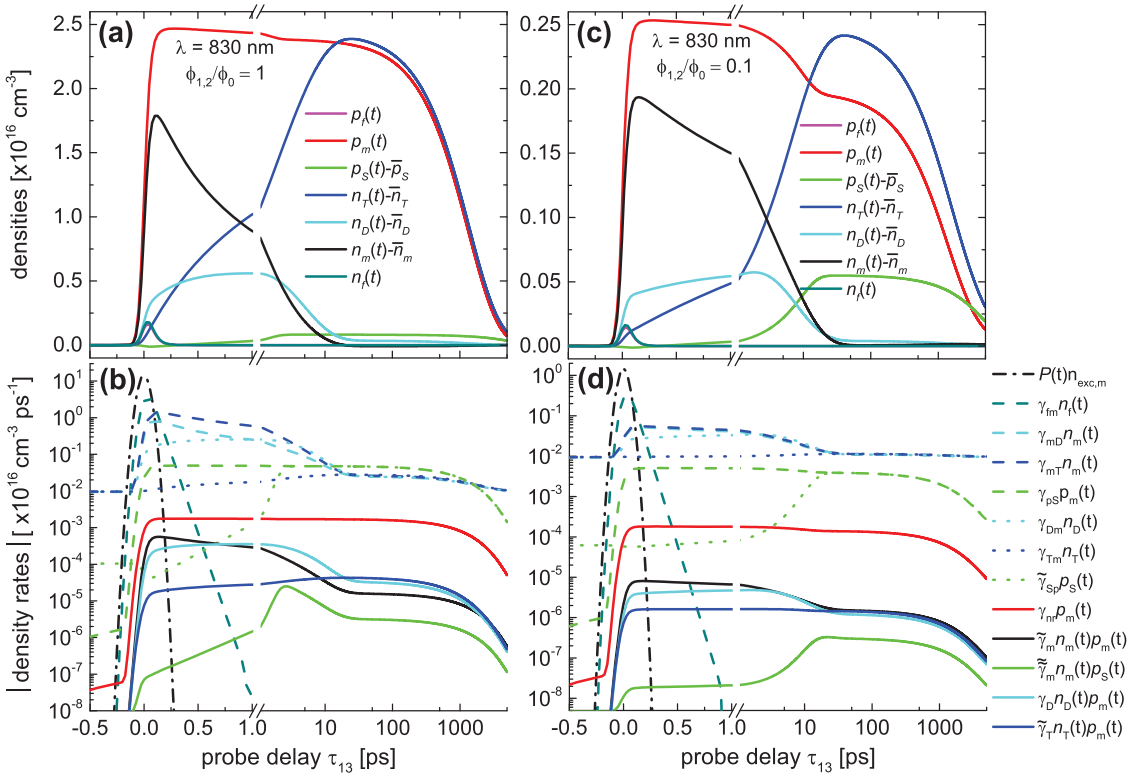

FIG. 12. Calculated dynamics of $n_f(t)$, $n_m(t)$, $n_D(t)$, $n_T(t)$, $p_S(t)$, $p_m(t)$, $p_f(t)$ for $T = 80$ K and an excitation wavelength of $\lambda = 830$ nm at (a) an excitation fluence $\phi_{1,2}/\phi_0 = 1$ and (c) at $\phi_{1,2}/\phi_0 = 0.1$ using Eq. (3). The corresponding density rates are given in (b) and (d), respectively. Processes of excitation (dash-dotted), relaxation (dashed), thermal activation (dotted), and recombination (solid), are given as labeled.

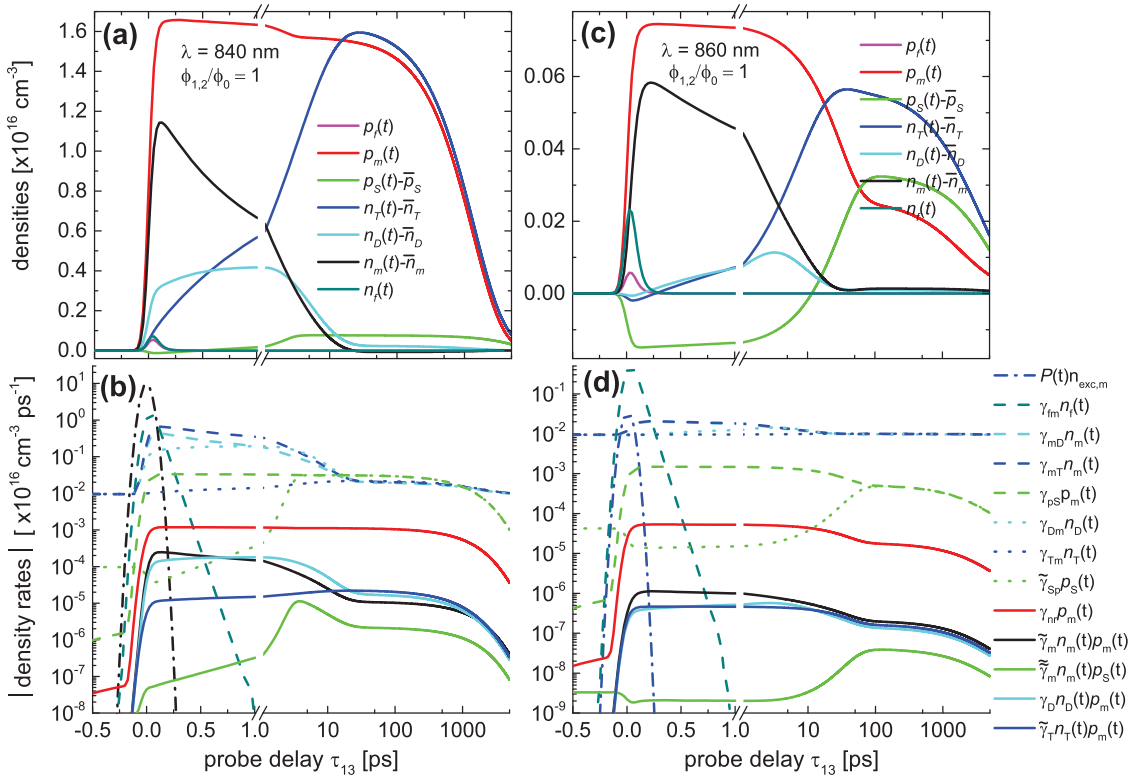

FIG. 13. As Fig. 12, but for (a) and (b) $\lambda = 840$ nm and (c) and (d) at $\lambda = 860$ nm at an excitation fluence $\phi_{1,2}/\phi_0 = 1$.

The coupled rate equations in Eq. (3) allow analyzing the dynamics of densities n_f, n_m, n_D, n_T, p_S, p_m, p_f. Figures 12(a) and 12(c) show an example of the calculated deviations of carrier densities from their equilibrium values and the density rates for $\Delta_M = 10$ meV at maximum pulse fluence $\phi_{1,2}/\phi_0 = 1$ and at lowest fluence $\phi_{1,2}/\phi_0 = 0.1$, respectively.

We discuss the results starting with $\phi_{1,2}/\phi_0 = 1$. The relaxation of the free electrons and holes is so fast that they relax within the excitation pulse duration to the mobility edge, and no significant free density builds up. The electrons at the mobility edge n_m relax within the first picoseconds into the donor n_D and trapped ZB states n_T. This decay corresponds to T_1 of 0.7 ps of the multiexponential fit [see Eq. (2)] to the population dynamics shown in Fig. 5. The corresponding absolute density rates $\tilde{\gamma}_{mD} n_m$ and $\gamma_{mT} n_m$ are shown in Fig. 12(b) as dashed cyan and blue lines. After about 1 ps, n_m is sufficiently depleted so that the n_D thermally activate into n_m and then relax into n_T. Thermal equilibrium in the conduction band, between n_m, n_T, and n_D, is reached after about 10 ps, as can be seen by the merging rates $\tilde{\gamma}_{mD} n_m$ and $\tilde{\gamma}_{Dm} n_D$, and of $\gamma_{mT} n_m$ and $\gamma_{Tm} n_T$, creating detailed balance. At about 3 ps, the surface trapped holes come into thermal equilibrium with the mobile holes, as can be seen by the merging of the trapping rate $\gamma_{pS} p_m$ and thermal activation rate $\tilde{\gamma}_{Sp} p_S$. The surface hole density p_S is close to the saturation density p_{S_0}. After intraband thermal equilibrium is established, the dynamics is dominated by the recombination of mobile holes. The nonradiative recombination is dominating (solid red line), as dictated by the low quantum yield of about 2% at this temperature. The radiative recombination is dominated by the electrons in the ZB sections and the donor states, consistent with the observed PL spectrum (see Fig. 2). The decay reduces the trapped hole density, which reduces the screening, and consequently decreases the thermally excited mobile hole density exponentially. This dramatically reduces the recombination for times above 1 ns.

Turning now to the results for $\phi_{1,2}/\phi_0 = 0.1$ shown in Figs. 12(c) and 12(d), the initial dynamics up to about 5 ps show a reduced decay rate due to the reduced carrier-carrier scattering. Importantly, since the photoexcited hole density p_m is smaller than the saturation density of surface holes p_{S_0}, the thermal activation is slower due to the larger activation energy, leading to a hole thermalization only after about 20 ps. The subsequent population dynamics on the nanosecond timescale are again governed by the nonradiative recombination between mobile electrons and holes, fed by thermal activation of trapped electrons n_T and holes p_S. It is slower due to the reduced screening of the surface trapping potential.

For excitation below the mobility edge, at $\Delta_M = -7$, -25, and -42 meV, the population dynamics essentially remain the same, but the decay rates are reduced due to the reduced interband excitation density. Figures 13(a) and 13(c) show as an example the dynamics of densities at fluences $\phi_{1,2}/\phi_0 = 1$ for $\Delta_M = -7$ and -42 meV, respectively, revealing decreasing initial decay rates of n_m and p_m. The reduced screening of the surface trapping potential leads to an increased hole thermalization time of $\sim$100 ps for $\Delta_M = -42$ meV and provides a slower recombination dynamics.

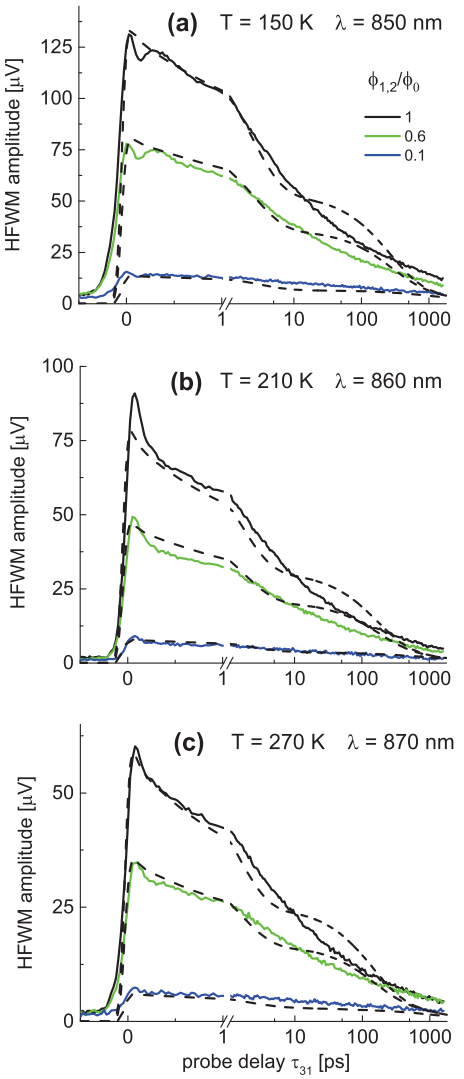

FIG. 14. Comparison of calculated HFWM (dashed black lines) obtained from Eqs. (3) and (4) with experimental data (full lines) at temperatures (a) $T = 150$ K, (b) 210 K, (c) 270 K and various excitation fluences $\phi_{1,2}/\phi_0$ as labeled.

The temperature dependence of the modeled dynamics is shown in Figs. 14(a)–14(c), giving the calculated HFWM amplitude and the experimental data obtained at 150, 210, and 270 K. Besides using the determined nonradiative rates γ_{nr} as a function of temperature (see Fig. 9), all other relaxation and bimolecular rate constants were kept equal to the $T = 80$ K calculations. For $T = 150$ K, we used $n_{\mathrm{exc},f} = 0$, $n_{\mathrm{exc},m} = 0.7 \times 10^{16}$ cm^{-3}, $n_{\mathrm{exc},D} = 0.26 \times 10^{16}$ cm^{-3}, and $n_{\mathrm{exc},T} = 0.15 \times 10^{16}$ cm^{-3} according to the pulse overlap with the exciton and donor transition bands. In addition, parameter C_T was adjusted to 0.5. At 210 and 270 K, we have $\Delta_M \sim -10$ meV, so that we used the same excitation densities and imaginary C parameters as for $\Delta_M \sim -7$ meV at $T = 80$ K. The C_T values were adjusted to 0.5 at $T = 210$ K and to 0.6 at $T = 270$ K. (A summary of the used parameters is shown in Table I). As mentioned earlier, the consideration of a distribution of ZB electrons with varying trapping energies and transition rates would likely lead to a

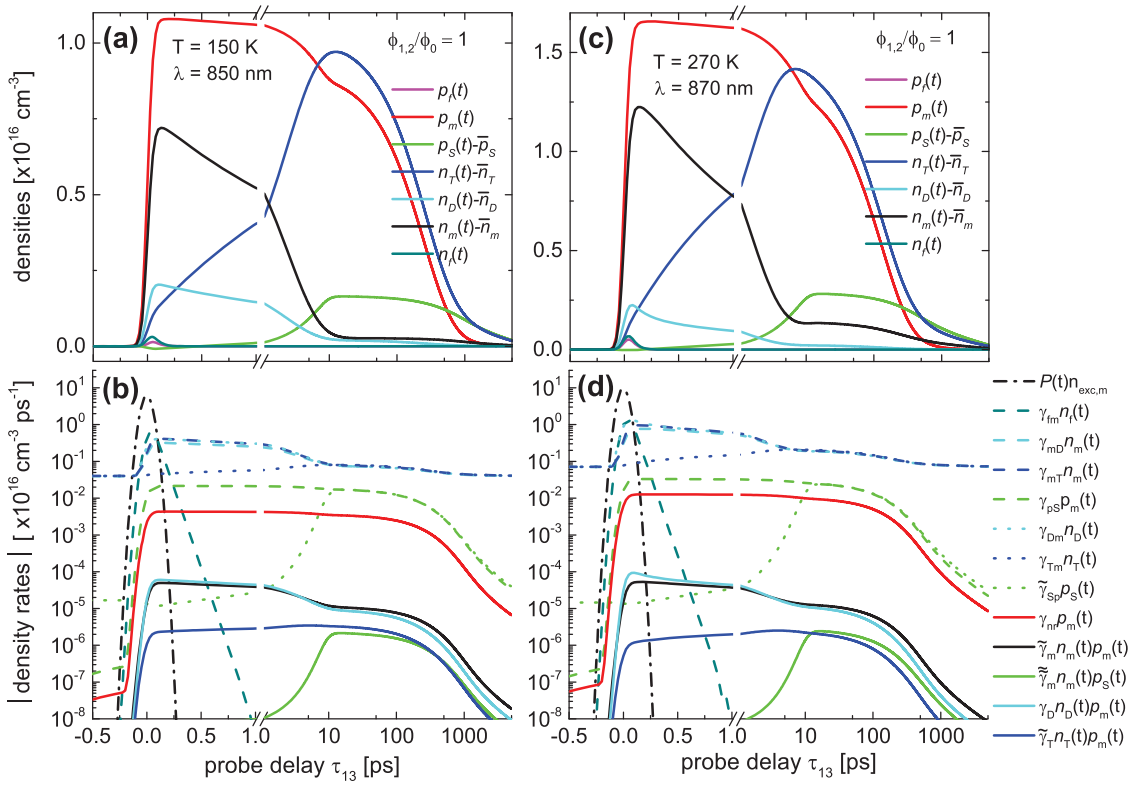

FIG. 15. As Fig. 12, but for (a) and (b) $T = 150\,\mathrm{K}$, $\lambda = 850\,\mathrm{nm}$ and (c) and (d) $T = 210\,\mathrm{K}$, $\lambda = 870\,\mathrm{nm}$ and an excitation fluence $\phi_{1,2}/\phi_0 = 1$.

better agreement between the calculation and the experimental data. The calculations also reproduce the data at lower pump pulse fluences [see Figs. 11(a)–11(c) for $F = 0.6$ and 0.1] using the same parameters as for $F = 1$ but increasing C_T values as shown in Table I.

The resulting densities n_f, n_m, n_D, n_T, p_S, p_m, p_f at different temperatures are shown in Figs. 15(a) and 15(c) for a fluence of $\phi_{1,2}/\phi_0 = 1$ for 150 and 270 K, and the corresponding density rates are given in Figs. 15(b) and 15(d). The main temperature dependence is a shortening of the thermalization times due to the faster thermally activated rates, yielding about 10 ps for electrons and holes at 150 K, and 5 ps at 300 K. Due to the large trapping energy of the surface holes, which is partially screened by the surface hole density, the longer dynamics remain remarkably independent on temperature, as there is an equilibrium density of surface holes established by the pulse repetition rate, which screens the trapping energy and thus modifies the thermally activated population of mobile holes, to adjust the average decay rate to match the average excitation rate.

IV. CONCLUSIONS

We studied the dephasing and population dynamics of e-h pairs in polytype InP NWs using three-beam HFWM, for excitation densities in the $10^{15}-10^{16}\mathrm{cm}^{-3}$ range and temperatures from 80 to 270 K. The population dynamics show processes with time constants spanning the full measured range of timescales, from 100 fs to 100 ns. With increasing excitation density, the faster components in the subnanosecond range get more prominent. The electron capture constant of about 5 ps is similar to the dynamics observed with PL up-conversion [38]. The intraband dynamics of excited background electrons originating from ionized donors with a density of about $10^{16}\mathrm{cm}^{-3}$ contributes to the initial dynamics of the HFWM amplitude. The longer dynamics in the nanosecond range is controlled by electron-hole separation due to surface band bending, and nonradiative recombination. Photon echo experiments at $T = 80\,\mathrm{K}$ reveal an exciton dephasing time of less than 100 fs, while a time of several hundred femtoseconds is expected. We attribute this shorter-than-expected dephasing time to exciton-carrier scattering, which is consistent with the typical donor concentration in these InP NWs in the order of $10^{16}\mathrm{cm}^{-3}$ [61].

ACKNOWLEDGMENTS

The authors acknowledge Dr. G. Duscher, Dr. O. Dyck, and Dr. M. Fickenscher for providing HRTEM images and fruitful discussion. The Australian Research Council (ARC) is acknowledged for its financial support, and the authors also acknowledge the use of facilities in the ACT node of the Australian National Fabrication Facility. Support from the Faculty Development Council (FDC) and the University Research Council (URC) at the University of Cincinnati is kindly acknowledged.

[1] X. Zhou, S. A. Dayeh, D. Aplin, D. Wang, and E. T. Yu, Appl. Phys. Lett. **89**, 053113 (2006).

[2] J. F. Wang, M. S. Gudiksen, X. F. Duan, Y. Cui, and C. M. Lieber, Science **293**, 1455 (2001).

[3] T. B. Hoang, L. V. Titova, J. M. Yarrison-Rice, H. E. Jackson, A. O. Govorov, Y. Kim, H. J. Joyce, H. H. Tan, C. Jagadish, and L. M. Smith, Nano Lett. **7**, 588 (2007).

[4] A. Mishra, L. V. Titova, T. B. Hoang, H. E. Jackson, L. M. Smith, J. M. Yarrison-Rice, Y. Kim, H. J. Joyce, Q. Gao, H. H. Tan, and C. Jagadish, Appl. Phys. Lett. **91**, 263104 (2007).

[5] R. S. Wagner and W. C. Ellis, Appl. Phys. Lett. **4**, 89 (1964).

[6] X. Duan and C. M. Lieber, Adv. Mater. **12**, 298 (2000).

[7] Q. Gao, H. H. Tan, H. E. Jackson, L. M. Smith, J. M. Yarrison-Rice, J. Zou, and C. Jagadish, Semicond. Sci. Technol. **26**, 014035 (2011).

[8] T. J. Trentler, K. M. Hickman, S. C. Goel, A. M. Viano, P. C. Gibbons, and W. E. Buhro, Science **270**, 1791 (1995).

[9] D. Xu, D. Chen, Y. Xu, X. Shi, G. Guo, L. Gui, and Y. Tang, Pure Appl. Chem. **72**, 127 (2000).

[10] Q. Gao, D. Saxena, F. Wang, L. Fu, S. Mokkapati, Y. Guo, L. Li, J. Wong-Leung, P. Caroff, H. H. Tan, and C. Jagadish, Nano Letters **14**, 5206 (2014).

[11] K. Tomioka, T. Tanaka, S. Hara, K. Hiruma, and T. Fukui, IEEE J. Sel. Top. Quantum Electron. **17**, 1112 (2011).

[12] M. Montazeri, M. Fickenscher, L. M. Smith, H. E. Jackson, J. Yarrison-Rice, J. H. Kang, Q. Gao, H. H. Tan, C. Jagadish, Y. N. Guo, J. Zou, M. E. Pistol, and C. E. Pryor, Nano Letters **10**, 880 (2010).

[13] Y. Masumoto, K. Goto, S. Yoshida, Y. Sakuma, P. Mohan, J. Motohisa, and T. Fukui, Phys. Rev. B **82**, 075313 (2010).

[14] S. Paiman, Q. Gao, H. H. Tan, C. Jagadish, K. Pemasiri, M. Montazeri, H. E. Jackson, L. M. Smith, J. M. Yarrison-Rice, X. Zhang, and J. Zou, Nanotechnology **20**, 225606 (2009).

[15] M. E. Reimer, M. P. van Kouwen, M. Barkelid, M. Hocevar, M. H. M. van Weert, R. E. Algra, E. Bakkers, M. T. Bjork, H. Schmid, H. Riel, L. P. Kouwenhoven, and V. Zwiller, J. Nanophotonics **5**, 053502 (2011).

[16] M. E. Reimer, M. P. van Kouwen, A. W. Hidma, M. H. M. van Weert, E. Bakkers, L. P. Kouwenhoven, and V. Zwiller, Nano Lett. **11**, 645 (2010).

[17] M. H. M. van Weert, N. Akopian, U. Perinetti, M. P. van Kouwen, R. E. Algra, M. A. Verheijen, E. Bakkers, L. P. Kouwenhoven, and V. Zwiller, Nano Lett. **9**, 1989 (2009).

[18] K. Pemasiri, M. Montazeri, R. Gass, L. M. Smith, H. E. Jackson, J. Yarrison-Rice, S. Paiman, Q. Gao, H. H. Tan, C. Jagadish, X. Zhang, and J. Zou, Nano Lett. **9**, 648 (2009).

[19] A. Maharjan, K. Pemasiri, P. Kumar, A. Wade, L. M. Smith, H. E. Jackson, J. M. Yarrison-Rice, A. Kogan, S. Paiman, Q. Gao, H. H. Tan, and C. Jagadish, Appl. Phys. Lett. **94**, 193115 (2009).

[20] N. Akopian, G. Patriarche, L. Liu, J. C. Harmand, and V. Zwiller, Nano Lett. **10**, 1198 (2010).

[21] D. Spirkoska, J. Arbiol, A. Gustafsson, S. Conesa-Boj, F. Glas, I. Zardo, M. Heigoldt, M. H. Gass, A. L. Bleloch, S. Estrade, M. Kaniber, J. Rossler, F. Peiro, J. R. Morante, G. Abstreiter, L. Samuelson, and A. Fontcuberta i Morral, Phys. Rev. B **80**, 245325 (2009).

[22] X. F. Duan, Y. Huang, R. Agarwal, and C. M. Lieber, Nature **421**, 241 (2003).

[23] D. Saxena, S. Mokkapati, P. Parkinson, N. Jiang, Q. Gao, H. H. Tan, and C. Jagadish, Nat. Photonics **7**, 963 (2013).

[24] H.-G. Park, C. J. Barrelet, Y. Wu, B. Tian, F. Qian, and C. M. Lieber, Nat. Photonics **2**, 622 (2008).

[25] A. Berg, S. Yazdi, A. Nowzari, K. Storm, V. Jain, N. Vainorius, L. Samuelson, J. B. Wagner, and M. T. Borgstrom, Nano Lett. **16**, 656 (2016).

[26] Y. Zhang, J. Wu, M. Aagesen, and H. Liu, J. Phys. D: Appl. Phys. **48**, 463001 (2015).

[27] H. T. Ng, J. Han, T. Yamada, P. Nguyen, Y. P. Chen, and M. Meyyappan, Nano Lett. **4**, 1247 (2004).

[28] M. H. M. van Weert, M. den Heijer, M. P. van Kouwen, R. E. Algra, E. Bakkers, L. P. Kouwenhoven, and V. Zwiller, Appl. Phys. Lett. **96**, 233112 (2010).

[29] M. P. van Kouwen, M. E. Reimer, A. W. Hidma, M. H. M. van Weert, R. E. Algra, E. Bakkers, L. P. Kouwenhoven, and V. Zwiller, Nano Lett. **10**, 1817 (2010).

[30] J. Heinrich, A. Huggenberger, T. Heindel, S. Reitzenstein, S. Hofling, L. Worschech, and A. Forchel, Appl. Phys. Lett. **96**, 211117 (2010).

[31] M. N. Makhonin, A. P. Foster, A. B. Krysa, P. W. Fry, D. G. Davies, T. Grange, T. Walther, M. S. Skolnick, and L. R. Wilsont, Nano Lett. **13**, 861 (2013).

[32] M. P. van Kouwen, M. H. M. van Weert, M. E. Reimer, N. Akopian, U. Perinetti, R. E. Algra, E. Bakkers, L. P. Kouwenhoven, and V. Zwiller, Appl. Phys. Lett. **97**, 113108 (2010).

[33] A. Othonos, E. Lioudakis, D. Tsokkou, U. Philipose, and H. E. Ruda, J. Alloys Compd. **483**, 600 (2009).

[34] H. J. Joyce, P. Parkinson, N. Jiang, C. J. Docherty, Q. Gao, H. H. Tan, C. Jagadish, L. M. Herz, and M. B. Johnston, Nano Lett. **14**, 5989 (2014).

[35] L. V. Titova, T. B. Hoang, J. M. Yarrison-Rice, H. E. Jackson, Y. Kim, H. J. Joyce, Q. Gao, H. H. Tan, C. Jagadish, X. Zhang, J. Zou, and L. M. Smith, Nano Letters **7**, 3383 (2007).

[36] T. T. T. Vu, T. Zehender, M. A. Verheijen, S. R. Plissard, G. W. G. Immink, J. E. M. Haverkort, and E. P. A. M. Bakkers, Nanotechnology **24**, 115705 (2013).

[37] S. Crankshaw, S. Reitzenstein, L. C. Chuang, M. Moewe, S. Münch, C. Böckler, A. Forchel, and C. Chang-Hasnain, Phys. Rev. B **77**, 235409 (2008).

[38] C. K. Yong, J. Wong-Leung, H. J. Joyce, J. Lloyd-Hughes, Q. Gao, H. H. Tan, C. Jagadish, M. B. Johnston, and L. M. Herz, Nano Lett. **13**, 4280 (2013).

[39] D. S. Chemla and J. Shah, Nature **411**, 549 (2001).

[40] W. Langbein, H. Gislason, and J. M. Hvam, Phys. Rev. B **60**, 16667 (1999).

[41] E. J. Mayer, J. O. White, G. O. Smith, H. Lage, D. Heitmann, K. Ploog, and J. Kuhl, Phys. Rev. B **49**, 2993 (1994).

[42] T. Baars, W. Braun, M. Bayer, and A. Forchel, Phys. Rev. B **58**, R1750 (1998).

[43] W. Braun, M. Bayer, A. Forchel, H. Zull, J. P. Reithmaier, A. I. Filin, and T. L. Reinecke, Phys. Rev. B **56**, 12096 (1997).

[44] H. P. Wagner, H.-P. Tranitz, W. Langbein, J. M. Hvam, G. Bacher, and A. Forchel, Physica Status Solidi B **231**, 11 (2002).

[45] H. P. Wagner, W. Langbein, J. M. Hvam, G. Bacher, T. Kummell, and A. Forchel, Phys. Rev. B **57**, 1797 (1998).

[46] H. P. Wagner, H.-P. Tranitz, R. Schuster, G. Bacher, and A. Forchel, Phys. Rev. B **63**, 155311 (2001).

[47] W. Langbein, Rivista del Nuovo Cimento **33**, 255 (2010).

[48] W. Langbein and B. Patton, J. Phys.: Condens. Matter **19**, 295203 (2007).

[49] M. Kaveh, G. Duscher, Q. Gao, C. Jagadish, and H. P. Wagner, Mater. Res. Express **2**, 045001 (2015).

[50] A. Naeem, F. Masia, S. Christodoulou, I. Moreels, P. Borri, and W. Langbein, Phys. Rev. B **91**, 121302 (2015).
[51] Y. T. Shih, W. C. Chiang, C. S. Yang, M. C. Kuo, and W. C. Chou, J. Appl. Phys. **92**, 2446 (2002).
[52] E. G. Gadret, M. M. de Lima, Jr., J. R. Madureira, T. Chiaramonte, M. A. Cotta, F. Iikawa, and A. Cantarero, Appl. Phys. Lett. **102**, 122101 (2013).
[53] S. Rudin, T. L. Reinecke, and B. Segall, Phys. Rev. B **42**, 11218 (1990).
[54] L. Zhang, J.-W. Luo, A. Zunger, N. Akopian, V. Zwiller, and J.-C. Harmand, Nano Lett. **10**, 4055 (2010).
[55] M. Murayama and T. Nakayama, Phys. Rev. B **49**, 4710 (1994).
[56] M. Gurioli, A. Vinattieri, J. Martinez-Pastor, and M. Colocci, Phys. Rev. B **50**, 11817 (1994).
[57] W. Langbein, S. Hallstein, H. Kalt, R. Notzel, and K. Ploog, Phys, Rev. B **51**, 1946 (1995).
[58] W. J. Turner, W. E. Reese, and G. D. Pettit, Phys. Rev. **136**, A1467 (1964).
[59] M. De Luca, A. Zilli, H. A. Fonseka, S. Mokkapati, A. Miriametro, H. H. Tan, L. M. Smith, C. Jagadish, M. Capizzi, and A. Polimeni, Nano Lett. **15**, 998 (2015).
[60] U. Strauss, W. W. Ruhle, and K. Kohler, Appl. Phys. Lett. **62**, 55 (1993).
[61] H. J. Joyce, C. J. Docherty, Q. Gao, H. H. Tan, C. Jagadish, J. Lloyd-Hughes, L. M. Herz, and M. B. Johnston, Nanotechnology **24**, 214006 (2013).
[62] D. S. Kim, J. Shah, J. E. Cunningham, T. C. Damen, W. Schafer, M. Hartmann, and S. Schmitt-Rink, Phys. Rev. Lett. **68**, 1006 (1992).
[63] L. Schultheis, J. Kuhl, A. Honold, and C. W. Tu, Phys. Rev. Lett. **57**, 1635 (1986).
[64] L. C. Andreani, A. Dandrea, and R. Delsole, Phys. Lett. A **168**, 451 (1992).
[65] M. S. Skolnick and P. J. Dean, J. Phys. C: Solid State Phys. **15**, 5863 (1982).